

Fractional-Monolayer 2D-GaN/AlN Structures: Growth Kinetics and UVC-emitter Applications

Valentin Jmerik, Dmitrii Nечаев, Евгений Европейцев, Евгений Рогинский, Мария Яговкина, Проктор Алеクсеев, Алексей Семенов, Владимир Козловский, Михаил Зверев, Никита Гамов, Тао Ван, Хиньцянг Ван, Татьяна Шубина, Алексей Торопов,*

V.N. Jmerik, D.V. Nечаев, E.A. Европейцев, E.M. Рогинский, A.N. Семенов,

M.A. Яговкина, P.A. Алеクсеев, T.V. Шубина, A.A. Торопов

Centre of Nanoheterostructure Physics, Ioffe Institute, 26 Politekhnicheskaya,

Saint Petersburg, 194021, Russia

E-mail: jmerik@pls.ioffe.ru

V.I. Козловский, М.М. Зверев, Н.А. Гамов

²Lebedev Physical Institute, Leninsky Avenue 53, Moscow 119991, Russia;

Tao Wang, Xinqiang Wang

³State Key Laboratory for Mesoscopic Physics and Frontiers Science Center for Nano-optoelectronics, School of Physics, Peking University, Beijing 100871, China

Funding: National Key R&D Program :Intergovernmental International Science and Technology Innovation Cooperation, Project №2022YFE0140100

Keywords: ((3–7 keywords, not capitalized, plural, separated by commas, no full stop))
group-III Nitrides, two-dimensinal structures, fractional monolayer, quantum wells, quantum ribbons, quantum disks, plasma-assisted molecular beam epitaxy, ultraviolet-C emitters

Abstract

The paper reports on fundamental properties of the GaN/AlN quantum wells (QWs) with nominal subcritical thicknesses of 0.75–2 monolayers (MLs). They are grown by plasma-activated molecular beam epitaxy, varying either the nominal thickness or the gallium-to-nitrogen flux ratio. In situ monitoring reveals difference in 2D nucleation and step-flow growth modes of the QWs. The emission characteristics of QWs with integer thicknesses of 1 and 2 MLs depend weakly on the growth mechanism. In contrast, the intensity and spectral position luminescence of QWs with fractional-ML thicknesses are determined by the growth mechanism. Using ab initio calculations, a phenomenological model is proposed that describes fractional-ML QWs either as arrays of 2D quantum disks or as arrays of 2D quantum ribbons, in cases where 2D nucleation or step-flow growth mechanisms predominate, respectively. This model is generally consistent with experimental data on photo- and cathodoluminescence of heterostructures with multiple (250×) GaN/AlN QWs. These heterostructures, when pumped by electron beam at an energy 12.5 keV with a maximum pulse current of 2 A, exhibit linear current dependences of optical peak powers up to 1 and 37 W for wavelengths of 228 and 256 nm, respectively, making them promising for use as powerfull ultraviolet-C emitters.

1. Introduction

In the 1970-80s, discovery of quantum-dimensional effects in optical materials led to the development of semiconductor quantum wells (QWs) by C.H. Henry^[1,2] and quantum dots (QDs) by A.I.Ekimov.^[3,4] Firstly, these quantum-sized structures improve the performance of light-emitting devices due to their relatively narrow density of state functions. Furthermore, the spatial localization of charge carriers in these objects with a smaller band gap compared to the surrounding barrier layers (matrix) mitigates the decrease in radiative recombination efficiency in these structures with increasing temperature and defect concentration.

A wide range of quantum-dimensional objects are formed using several basic growth mechanisms of the heterostructures classified by Bauer in 1958.^[5] According to this classification, the two-dimensional (2D) Frank-de-Merwe growth mechanism, realized in crystallographically matched or slightly mismatched (<1%) heterostructures, ensures the epitaxial growth of QWs with a typical thickness of several nanometers. Otherwise, the three-dimensional (3D) Volmer-Weber growth mechanism in the highly mismatched heterostructures (>10%) results in formation of relatively large 3D objects. In the case of moderately crystallographically mismatched heterostructures, the growth of QDs becomes possible due to the so-called Stranski-Krastanov mechanism in such heterostructures.^[6] With such a two-stage 2D/3D growth, the initial accumulation of elastic energy to a critical thickness with a typical value of 1–2 monolayers (MLs) ensures the transition from 2D to 3D growth of QDs with characteristic dimensions in the nanometer range.

The first GaN QDs in an AlN matrix were grown by B. Daudin's group in 1997 using the Stranski-Krastanov growth mechanism in plasma-activated MBE (PA MBE).^[7–10] Various GaN/Al(Ga)N QDs were grown by several groups using the same approach,^[11–16] as well as ammonia MBE (NH₃-MBE),^[17,18] metalorganic chemical vapor deposition (MOCVD).^[19,20] Droplet epitaxy was developed to form GaN QDs using either NH₃-MBE^[21] or MOCVD.^[22] The typical thickness of these QDs of 1–7 nm ensures quantum confinement of charge carriers, since their photoluminescence (PL) or cathodoluminescence (CL) spectra exhibit UV emission with energies exceeding the GaN band gap of 3.4 eV. In most studies, the radiation energy does not exceed 4 eV, and only in some studies^[9,18,22] the observed higher values of up to ~5 eV were attributed to the ML-thick wetting GaN layer. The most important advantage of GaN/AlN QDs compared to AlGaN-based QWs is not only their increased quantum efficiency due to the usual carrier localization, but also with the weakening of the so-called quantum confined Stark effect (QCSE) that occurs in hexagonal (wurtzite) III-N heterostructures due to the presence of strong polarization fields.^[8,14,15,23]

One of the most important areas of modern physics and technology of low-dimensional structures is the development of 2D-layers of various materials. First, graphene discovered in 2004 by A. Geim and K. Novoselov,^[24] is being actively researched both for its application in van der Waals epitaxy and for the development of new types of electronic and optoelectronic devices.^[25] Furthermore, 2D-dichalcogenides, disulfides, and III-nitrides, have been intensively explored.^[26,27] In addition to standard 2D- materials with planar topology, there is a certain interest in 2D-nanoribbons of various materials with a width of < 50 nm, discovered in 1996 by M. Fugita,^[28] and the physicochemical properties of which differ significantly from those of their planar counterparts.^[29] Although most studies are devoted to graphene 2D-nanoribbons, there are studies on other materials, including GaN, AlN, and related heterostructures.^[30]

In addition to the research areas described above, K. Ploog's group demonstrated in the early 1990s the capabilities of MBE to grow InAs islands with nominally subcritical thicknesses on the GaAs layers grown on vicinal substrates.^[31] These objects, called sub-ML or fractional ML QDs, have been realized in various semiconductors and have attracted attention from both their fundamental optical properties and the development of new types of photodetectors, light-emitting devices, and solar cells.^[32-34]

The trend of thinning active regions in light-emitting devices to the ML level has also extended to III-N-based devices. In the early 1990s, M.A. Khan proposed replacing the AlGaN layers in UV optoelectronic devices with ultra-short-period (several MLs-range with a GaN ML thickness of 0.259 nm) GaN/AlN superlattices, the so-called digital alloys.^[35] After first demonstrating this approach using MOCVD, S. Nikishin's group successfully fabricated digital alloy-based UVC LEDs using NH₃-MBE in the early 2000s.^[36,37]

In 2008, a sub-ML discrete PA MBE for fabrication of UV-emitting heterostructures with active regions in the form of ultrathin (<1ML) GaN QWs in AlGaN barrier layers was proposed by our group.^[38,39] Then, theoretical studies by Kamiya et al.^[40] and Strak et al.,^[41] as well as experimental work by Taniyasu et al.^[42] demonstrated the capabilities of ML-thick GaN/AlN QWs to significantly suppress QCSE as well as completely eliminate the detrimental TE/TM switching of the UVC output polarization mode in Al-rich AlGaN. Over the past decade, UVC- emitting ML-thick GaN/Al(Ga)N QW structures have been grown using both PA MBE^[43-56] and MOCVD.^[57-61] In thematic reviews,^[62,63] a general tendency for these structures to decrease the emission wavelength to a minimum of ~220–230 nm with a decrease in the nominal QW thickness to 1 ML or less has been noted. However, a systematic comparison of the radiative properties for different QW configurations remain lacking.

In this paper, we study both the 2D-nucleation and the step-flow growth mechanisms of GaN QWs with subcritical thicknesses (up to 2 ML) on ML-stepped AlN surfaces under various PA MBE growth conditions. A comprehensive study of $250 \times \{\text{GaN}_m/\text{AlN}_n\}$ multiple QWs (MQW) structures (where $m = 0.75 - 2$, $n = 15$ – thicknesses of GaN and AlN layers in MLs, respectively) using X-ray diffraction and X-ray reflectance at grazing angles, atomic force microscopy and scanning transmission electron microscopy confirm not only their high structural quality, but also the controlling the nominal QW's thickness with an accuracy of 0.25 ML. In parallel, ab initio calculations of the electronic structures of GaN/AlN QWs with various ML and bilayer (BL) well configurations are performed. Based on the results of these calculations and analysis of the PL and CL spectra of the two series of MQW structures, a phenomenological model is developed that describes the relationship between the 2D-growth modes of these MQW structures with the formation of quantum disks and/or quantum ribbons, emitting in the UVC spectral range of 228 – 260 nm with various intensity. As a result, electron-beam-pumped UVC emitters with output peak optical powers of up to several tens of watts are demonstrated.

2. Main 2D-growth modes of monolayer-thick GaN/AlN quantum wells

The growth kinetics of ML-thick GaN QWs was studied during their growth on the AlN top layers of $250 \times \{\text{GaN}_{1.5}/\text{AlN}_{15}\}$ MQW structures, which have a stepped relief in the form of hexagonal spiral mounds with atomically smooth terraces with a typical width $\omega_t = 30 - 40$ nm and a typical step height of 1–2 MLs. The basic principles of growth of these structures using PA MBE on *c*-sapphire substrates was described by us previously,^[46,49,50] and their analysis will be continued in the next sections.

Figure 1a shows that the RHEED images retain a streaky pattern during the growth of all 1.5-ML-thick GaN layers, which is generally consistent with the subcritical thickness of these GaN layers (<2 ML) (see Refs. 10,13,64 and also with our measurements shown in Figure S1). Meanwhile, analysis of the temporal variations of the specular RHEED intensity (hereinafter referred to as “RHEED intensities”) reveals their strong dependence on the flux ratio $\phi_{\text{Ga}}/\phi_{\text{N}2*} = 0.7 - 2.1$). Several factors can determine the evolution of RHEED intensity during the initial growth of GaN on a 2D-AlN surface.^[65] Firstly, the RHEED intensity decreases due to the change in the average internal potential of the subsurface region from 14.23 eV (AlN) to 16.82 eV (GaN).^[66] Furthermore, the stronger and faster decrease in RHEED intensity observed when growing GaN under Ga-rich growth conditions is apparently due to the excess Ga accumulated on the surface, which enhances electron beam scattering. Both of these

factors lead to a monotonic decrease in RHEED intensity, ultimately reaching a lower constant level upon transition to the average GaN composition and the formation of a thermodynamically stable Ga BL in accordance with Northrup and Neugebauer model.^[67] The experimental facts confirm the accumulation of Ga excess under Ga-enriched conditions. First, the RHEED intensity showed reverse changes after growth, indicating the desorption of Ga excess at the growth temperature of 690°C.^[68] In addition, the AFM image of surface of 1.5 ML-thick GaN layer grown under $\phi_{\text{Ga}}/\phi_{\text{N}2*} = 2.1$, shown in Figure 1f, reveals clusters having a thickness of 1–2 nm and a typical lateral size of about 15 nm. The estimated total volume of these nanoclusters is approximately equal to the volume of Ga excess with a nominal thickness of 1.5ML formed during the growth of a 1.5ML-thick GaN layer (Figure S2). The nanoclusters appear after GaN growth with a rapid temperature drop due to the dewetting phenomenon, which is a thermodynamically driven transition from a continuous Ga adlayer to the Ga nanocluster phase.^[69] Note that the AFM image of a GaN layer grown at the same thickness with $\phi_{\text{Ga}}/\phi_{\text{N}2*} = 1.1$ shows no signs of the metal excess (Figure 1e).

The third factor determining the behavior of the RHEED intensity is related with the evolution of the surface morphology during layer-by-layer growth of GaN in accordance with one of two possible 2D growth mechanisms, schematically shown in Figure 1b. During 2D-nucleation growth mode, the RHEED intensity oscillates with a period corresponding to the growth of one ML as the surface is successively filled with 2D-islands, which leads to a periodic change in the area of the lateral boundaries of islands, effectively scattering the electron beam.^[65,70] On the contrary, the effective surface diffusion of adatoms to the step edges in the step-flow growth mechanism leads to a constant density of scattering edges, which determines the absence of RHEED oscillations.

Figure 1a shows that the RHEED intensity factors play different roles in the GaN growth process under different conditions. During GaN growth under nitrogen-rich conditions and unit stoichiometric conditions ($\phi_{\text{Ga}}/\phi_{\text{N}2*} = 0.7$ and 1.1, respectively) the RHEED intensities exhibit a kink in the linear decrease at the time corresponding to the growth of the initial 0.5 ML GaN layer. In contrast, when these layers are grown under metal-rich conditions ($\phi_{\text{Ga}}/\phi_{\text{N}2*} \geq 1.6$), the RHEED intensity varies linearly without any kink. Therefore, the observed kink at the initial growth stage can be explained by the addition of a third oscillating factor in the linear change of the RHEED intensity, as illustrated in Figure S3.

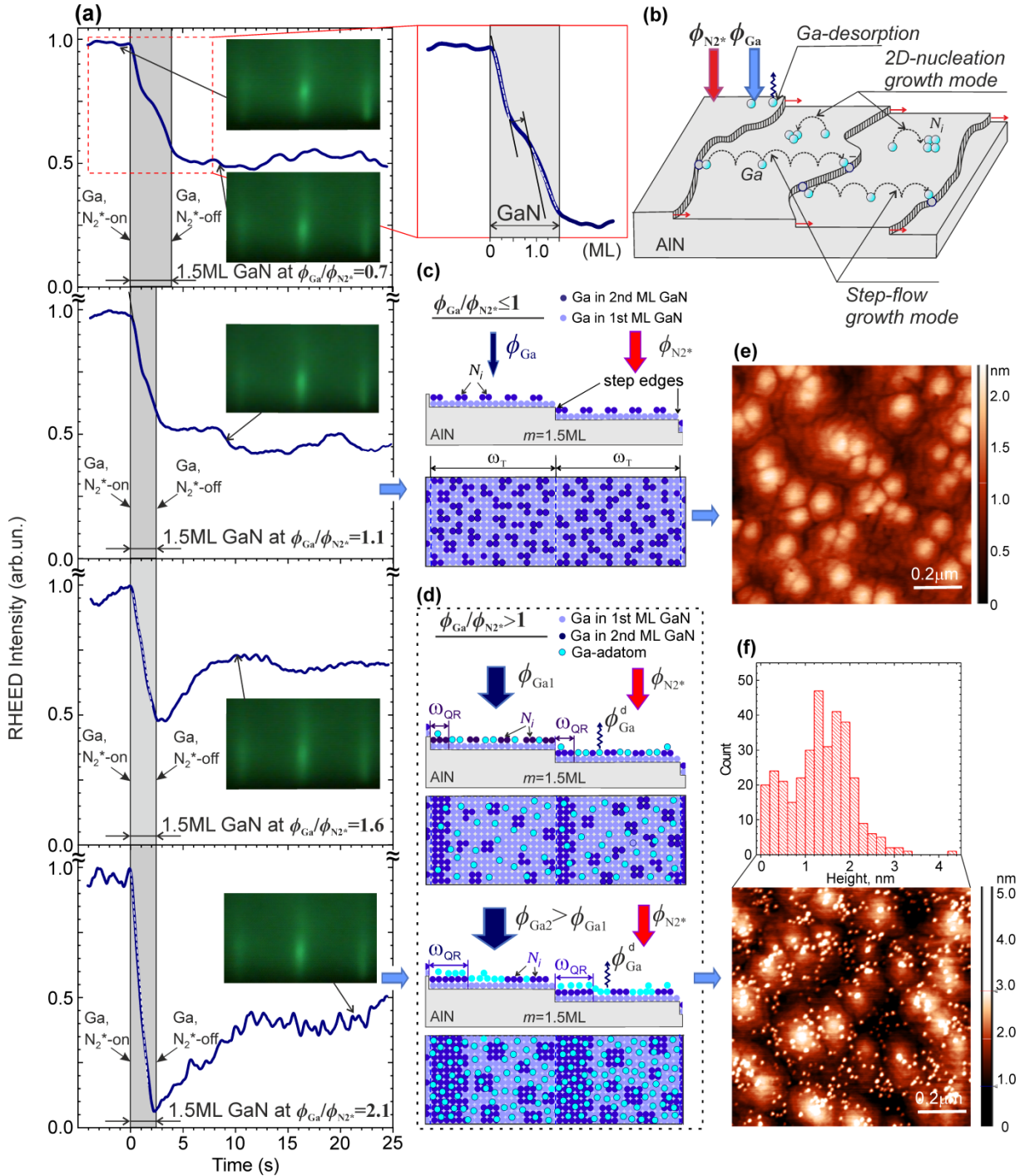


Figure 1. (a) Time evolution of RHEED specular reflectance intensity during growth of 1.5-ML-thick GaN layer on AlN layers at different $\phi_{\text{Ga}}/\phi_{\text{N}_2^*} = 0.7 – 2.1$. (b) Schematic illustration of the main growth modes of GaN on a stepped AlN layer, including 2D-nucleation and step-flow growth mechanisms. Surface structures of GaN QWs with a nominal thickness of 1.5ML grown at the different $\phi_{\text{Ga}}/\phi_{\text{N}_2^*}$: < 0.7 (c) and > 1 (d). N_i , ω_T and ω_{QR} –see in text. AFM images ($1 \times 1 \mu\text{m}^2$) of 1.5ML-thick GaN grown at different $\phi_{\text{Ga}}/\phi_{\text{N}_2^*}$: 1.1 (e) and 2.2 (f). The inset in (f) shows a histogram of the of Ga cluster height values.

From a physical point of view, the observation of oscillating RHEED intensity indicates that the limited surface mobility of Ga-adatoms (D) at low $\phi_{\text{Ga}}/\phi_{\text{N}2^*} < 1.1$ leads to the growth of each ML in a 2D-nucleation mode with an oscillating perimeter of the lateral edges of growth ML-thick islands as shown in Figure 1c. In principle, the kinetics of nucleation and further development of growth islands during the layer-by-layer GaN growth can be described by numerical model including three elementary processes of Deposition, Diffusion and Aggregation (DDA).^[71] These processes are mainly determined by the characteristic ratio $R=\phi_{\text{Ga}}/D$, which, in particular, controls the surface concentration of growth islands $N_i \sim R$ during the initial growth of each GaN ML (i.e. when the degree of the surface with Ga-adatoms $\theta \ll 1$). This mechanism will lead to the formation of GaN 2D-quantum dots (or disks) (2D-QDs) with a ML thickness at $m < 1$, which will apparently increase to the BL thickness during the growth of the second ML at $m = 1 - 2$.

Upon transition from nitrogen-enriched to metal-enriched growth conditions ($\phi_{\text{Ga}}/\phi_{\text{N}2^*} > 1.6$), the increasing of adatom surface mobility leads to a transition from 2D-nucleation to a step-flow growth mechanism of GaN in accordance with the Burton-Cabrera-Frank theory.^[72] Assuming layer-by-layer growth of a fractional ($2 > m > 1$) QW in this regime, after the first lower ML is completely filled, during the growth of the second layer, the directed diffusion of adatoms to the edges of the steps will lead to the formation of BL-thick unidirectionally elongated quantum-ribbon-like (QR) GaN objects at the steps, as shown in Figure 1d. The width of these QRs (ω_{QR}) is proportional not only to the nominal QW thickness, but also to the flux ratio $\phi_{\text{Ga}}/\phi_{\text{N}2^*}$, since increasing ϕ_{Ga} accelerates the transport of adatoms towards the step edges, as shown in the bottom panel in Figure 1d.

Finally, it should be taken into account that 100% implementation of one of the two mentioned growth mechanisms of GaN can most likely be observed only for the 2D nucleation regime at low $\phi_{\text{Ga}}/\phi_{\text{N}2^*}$ values (nitrogen-rich conditions) (Figure 1c). However, with increasing $\phi_{\text{Ga}}/\phi_{\text{N}2^*}$, the growth kinetics become significantly more complex and the formation of GaN MLs will be determined additionally by several 2D growth mechanisms, including spiral growth and step-flow mechanisms. Such a complex growth regime was described for the MOCVD growth of AlInGaN layers under highly nonequilibrium conditions.^[73] Since the PA MBE is also extremely far from equilibrium growth conditions, the above-stated manifestations of several mechanisms can be expected in it as well. As a result, at an insufficiently high $\phi_{\text{Ga}}/\phi_{\text{N}2^*}$ ratios, parasitic nucleation of 2D GaN QDs on atomic terraces will be associated with low adatom mobility, whereas at too high $\phi_{\text{Ga}}/\phi_{\text{N}2^*}$ ratios, enhanced nucleation of GaN on atomic terraces will occur due to increased Ga supersaturation.

Thus, in practice, at elevated surface concentrations of Ga-adatoms in Ga-rich conditions, a mixed growth mechanism can be expected, leading to the simultaneous formation of both 2D-QDs and 2D-QRs, as shown in Figure 1d. This discussion is continued in Section 6.

3. Ex situ studies of structural properties ML-thick GaN/AlN multiple quantum wells

3.1. Atomic Force Microscopy

Figure 2 and S4 show AFM images of $250 \times \{\text{GaN}_m/\text{AlN}_{15}\}$ MQW structures from the *T*- and *F*- series, respectively, with 15ML-thick AlN top layers, described in experimental section. Almost all images exhibit atomically smooth terrace-like surface topography with Root Mean Square (RMS) roughness in the range of 0.3-0.4 nm over an area $1 \times 1 \mu\text{m}^2$, terrace width of 30–40 nm, and height of 1–2 MLs (Figure S5). Only one structure in the *T*-series with the largest $m = 2$ ML near the critical thickness of the 2D-3D transition exhibits a surface with an increased RMS roughness of 0.69 nm without ML terrace signs. However, all structures in both growth series continuously exhibited a streaky RHEED pattern during throughout MQW structure growths.

Although most of the samples were grown under metal (Al and Ga)-rich conditions, their AFM, optical and scanning electron microscope images (Figure S6), exhibit no evidence of an excess surface metallic phase similar to that shown in Figure 1f. This indicates that Al excess accumulated during the growth of AlN barrier layers is completely consumed during the surface exposition under N_2^* flux prior to the growth of each QWs. Then, Ga excess accumulated during GaN QW growth is completely segregated and desorbed during the subsequent growth of AlN barrier layers, as analyzed in detail in our previous work.^[50] Moreover, it can be speculated that excess Ga atoms cannot be incorporated in AlN due to the lower cohesive energy of the Ga–N bond (2.20 eV) compared to Al–N (2.88 eV).^[74]

AFM measurements over the bigger scanning area of $5 \times 5 \mu\text{m}^2$ of the structures from both series have revealed relatively small increase of their RMS roughness to ~ 0.50 nm in the most structures and to ~ 1.0 nm for the *T*-2ML structure. This indicates the stable step-flow growth mechanism throughout $250 \times$ periods of the MQW-structures without any signs of step bunching. These observations are consistent with the data of Kaufmann et al.,^[75] who demonstrated the advantage of PA MBE under metal-rich conditions for suppressing the Ehrlich-Schwobel barrier,^[76] which serves as one of the driving forces of step bunching.

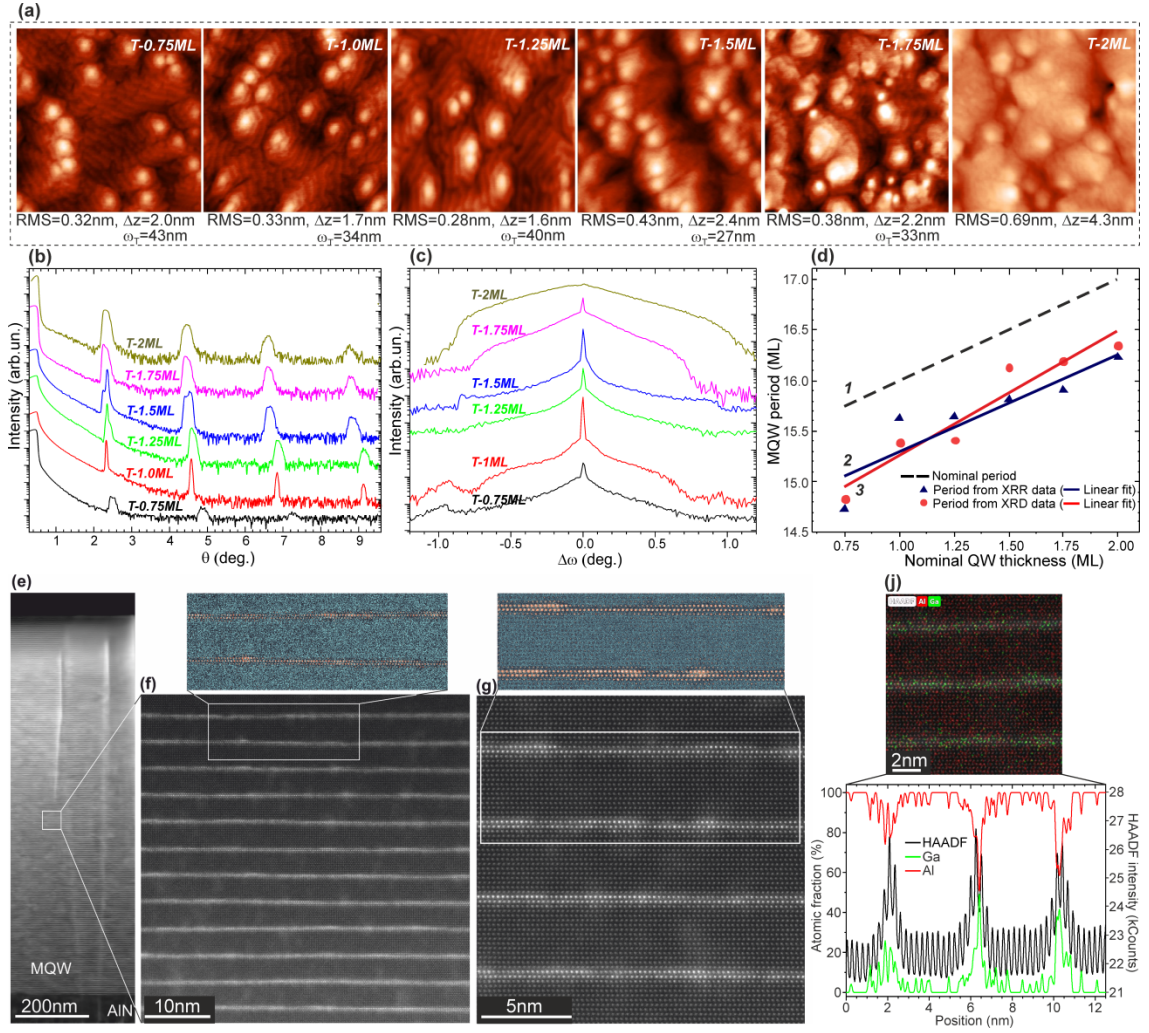


Figure 2. (a) AFM images ($1 \times 1 \mu\text{m}^2$) of the top AlN surfaces of MQW structures from the T -series. (b,c) θ - and ω -scans of the small-angle X-ray reflection curves for the T -series samples, respectively. (d) Dependences of the period of MQW structures on well thickness: (1) - nominal dependence, (2) and (3) – linear fits of the period values based on experimental XRR and XRD data, respectively. (e-g) HAADF-STEM images of the MQW structure $F-1.6$ with different magnifications. The insets in (f, g) show color enhanced images of the structure in the marked areas. (j) Combined HAADF-STEM and elemental mapping images of Ga and Al atoms obtained from energy dispersive X-ray spectroscopy data.

3.2. X-ray diffraction and X-ray reflection

The MQW structures were investigated also using measurements of X-ray diffraction (XRD) $\theta/2\omega$ -scans of symmetric reflections (0002) (Figure S7), as well as X-ray reflectometry (XRR) curves and small-angle scattering curves, shown in Figure 2b and c respectively. Table 1 compares the nominal and experimental values of the main MQW parameters ($m, n, T_{\text{SL}} = m+n$) estimated from XRD and XRR data, which are denoted by the superscripts $^{\text{nom}}$, $^{\text{XRD}}$ and $^{\text{XRR}}$, respectively.

TABLE 1. Parameters of T-series structures simulated from XRD $\theta/2\omega$ scans and XRR curves

m	T-0.75	T-1.0	T-1.25	T-1.5	T-1.75	T-2.0
T_{SL}^{nom} (ML)	15.75	16.0	16.25	16.5	16.75	17.0
m^{XRD} (ML)	0.502	0.490	0.394	0.590	0.707	1.07
n^{XRD} (ML)	14.337	14.904	15.020	15.542	15.490	15.273
T_{SL}^{XRD} (ML)	14.839	15.394	15.414	16.132	16.197	16.343
T_{SL}^{XRR} (ML)	14.739	15.635	15.639	15.807	15.904	16.225
RMS^{surf} (nm)	-	0.04	0.06	0.13	0.22	-
L^{lat} (nm)	-	29.2	34.8	10.2	11.1	5
L^{vert} (nm)	-	-	-	-	4	-

The summary Figure 2d shows that both X-ray methods estimate the MQW period and its relative change with increasing nominal QW thickness quite accurately, and discrepancies between the nominal and simulated values are less than $\sim 5\%$. However, the accuracy of determining the absolute values of the QW's and barrier layer's thicknesses is significantly lower, as has been discussed in our previous work.^[50] Briefly, this can be explained by both the fractional filling of the GaN atomic layers and the difficulty of correctly modeling the ML interface region between GaN and AlN atomic planes.^[77,78]

Nevertheless, despite the difficulties described above, both X-ray methods allow us to determine the MQW period variation in the fractional range of $m = 0.75\text{--}2\text{ML}$ with sufficient accuracy, and its continuous increase can be considered as a gradual transition from the growth of structures with predominantly ML-thick QWs to the growth of structures with a predominance of BL-thick QWs. Furthermore, Table 1 presents the results of modeling the morphology characteristics of the MQW structures using their experimental XRR curves. First, we note that the RMS surface roughness (RMS^{surf}) of the structures range from 0.04 to 0.22 nm, which are even yield slightly lower numerical values for this parameter measured by AFM. Figure 2c shows a gradual transformation of the $\Delta\omega$ scan shape from the sharpest peak in the $T\text{-}1.0\text{ML}$ structure to its almost complete disappearance in the $T\text{-}2.0\text{ML}$ structure with a thickness slightly smaller than the critical thickness for the transition from 2D to 3D surface morphology ($\sim 2.4\text{ML}$) in GaN/AlN QWs observed by RHEED (Figure S1).

Simulation of the XRR scans revealed lateral correlation lengths (L^{lat}) in the range of 10–35 nm, which roughly corresponds to the width of the atomically flat terraces of MQW structures. Higher values of L^{lat} were found for structures with a more pronounced stepped relief in AFM images (Figure 2a). Simulation also revealed the presence of a vertical correlation length $T^{SL} \geq 4$ nm only in one $T\text{-}1.75\text{ML}$ structure with a m value close to the critical thickness and a weakly defined stepped relief. The absence of the vertical correlation

in other MQW structures is explained by the stepped MQW morphology, which complicates the matching of height profiles during XRR curve analysis.

3.3. Scanning transmission electron microscopy

Figure 2e–g shows the HAADF-STEM images of the $250 \times \{\text{GaN}_{1.5}/\text{AlN}_{15}\}$ MQW structure from *F*-series (*F-1.6*), in which the z-contrast makes the Ga atoms with higher atomic masses appear brighter compared to the Al atoms. The determined from these images values of the average MQW period correspond to the nominal value $T_{\text{SL}}^{\text{nom}} = 41.235\text{\AA}$ with an accuracy of less than 2%, which corresponds to the non-uniformity of the MBE fluxes in the PA MBE setup. Importantly, GaN QWs exhibit a 2D-topography with the same period throughout the $250 \times$ period structure with a total thickness of more than $1\text{ }\mu\text{m}$. All the threading dislocations observed in the MQW structure (Figure 2e) originate from the AlN/c- Al_2O_3 buffer layer and no generation of new defects in the MQW structure was observed.

When analyzing HAADF-STEM images, it is necessary to take into account the specimen thickness of about 50 nm, which is necessary to obtain sufficient image intensity. On the other hand, in the case of the step-flow growth mechanism of the MQW structures, the planarity of the atomic layers is disrupted at distances exceeding the atomic terrace width ($> \omega_T$). This can lead to the observation of multiple atomic planes of Ga and to an incorrect estimate of the number of MLs in the GaN QWs. This effect is enhanced with increasing specimen thickness, and, therefore, can vary across a specimen in the case of thickness gradient, which typically occurs during specimen preparation for HAADF-STEM. Figure 2f shows a small-scale HAADF-STEM image of the MQW structure, in which the thickness of the GaN QWs appears to be greater in the lower part of the image, where specimen thickness is greater, compared to the upper part, in which this type of thickness error should be smaller.

HAADF-STEM image analysis confirms the presence of 1-ML-high atomic steps in Ga atomic layers, forming 2D-GaN regions of both ML and BL thicknesses in the AlN matrix, consistent with the step-flow and 2D-nucleation growth mechanisms. The typical lateral size of 2D-BL-GaN regions varies from several to tens of nanometers. At this stage of the study, it is difficult to assess the topology of the regions and the specific mechanism of their formation. This task is complicated by the complex topography of AlN barrier layers, consisting of hexagonal mounds with varying terrace widths and heights (Figure 2a), and the expected mixed growth mode of GaN QWs, consistent with both 2D-growth mechanisms (Figure 1b). Figure S8 presents the preliminary results of the simulation of the HAADF-STEM images of ML-, BL-, and fractional-ML GaN_m/AlN ($m = 1-2$) QWs with a terrace width of 40 nm.

4. Electronic properties of monolayer GaN/AlN quantum well structures

The theoretical description of the optical properties of III-N heterostructures is most often carried out either within the framework of density functional theory (DFT) or using a more resource-intensive quasiparticle approximation using the Green's function (G_0W_0).^[79] An accurate description of the electronic structures of these heterostructures using the first method is problematic, since the electronic states in the conduction band are determined with an accuracy of up to a constant due to the discontinuity of the derivative of the total energy in the forbidden gap.^[80] Therefore, G_0W_0 method was used for an accurate quantitative calculation of the electronic structure of the $\text{GaN}_m/\text{AlN}_n$ MQW structures ($m = 1, 2$; $n = 11, 12$). The calculated effective band gap values (E_g^*) were then used to construct a scissors operator to improve the accuracy of calculations of the electronic properties of the QW structures with different configurations, evaluated within less resource-intensive DFT method. The accuracy of both methods was verified by comparing the calculated and measured bandgaps of several $\text{GaN}_m/\text{AlN}_n$ ($m = 1.5-18$, $n = 3-16$) superlattices (SLs), as shown in Figure S9.^[81]

First, the electronic structures of the $\text{GaN}_m/\text{AlN}_n$ SLs with various m and n values were calculated using G_0W_0 method. **Figure 3a** shows the band structure for $\text{GaN}_8/\text{AlN}_8$ symmetric superlattice, those $E_g^* = 3.2$ eV is close to that of bulk GaN (3.4 eV). Figures 3b and c show that with a decrease in m to 2 and 1, successive increase in E_g^* by 1.2 and 0.5 eV is observed, respectively. According to these calculations and taking into account the systematic error of the G_0W_0 method (0.2 eV), the E_g^* values in the $\text{GaN}_1/\text{AlN}_{11}$ and $\text{GaN}_2/\text{AlN}_{11}$ MQW structures are 4.945 and 4.434 eV respectively. These results are generally consistent with the theoretical and experimental data.^[40,41,44,62,63] Calculations of electronic properties of the same MQW structures using the DFT method show the values of $E_g^* = 3.719$ and 3.174 eV, respectively. The similar values (0.511 and 0.548 eV) of the E_g^* difference between ML- and BL-thick QW structures, determined by both methods allowed the less resource-intensive DFT method to be used in further calculations.

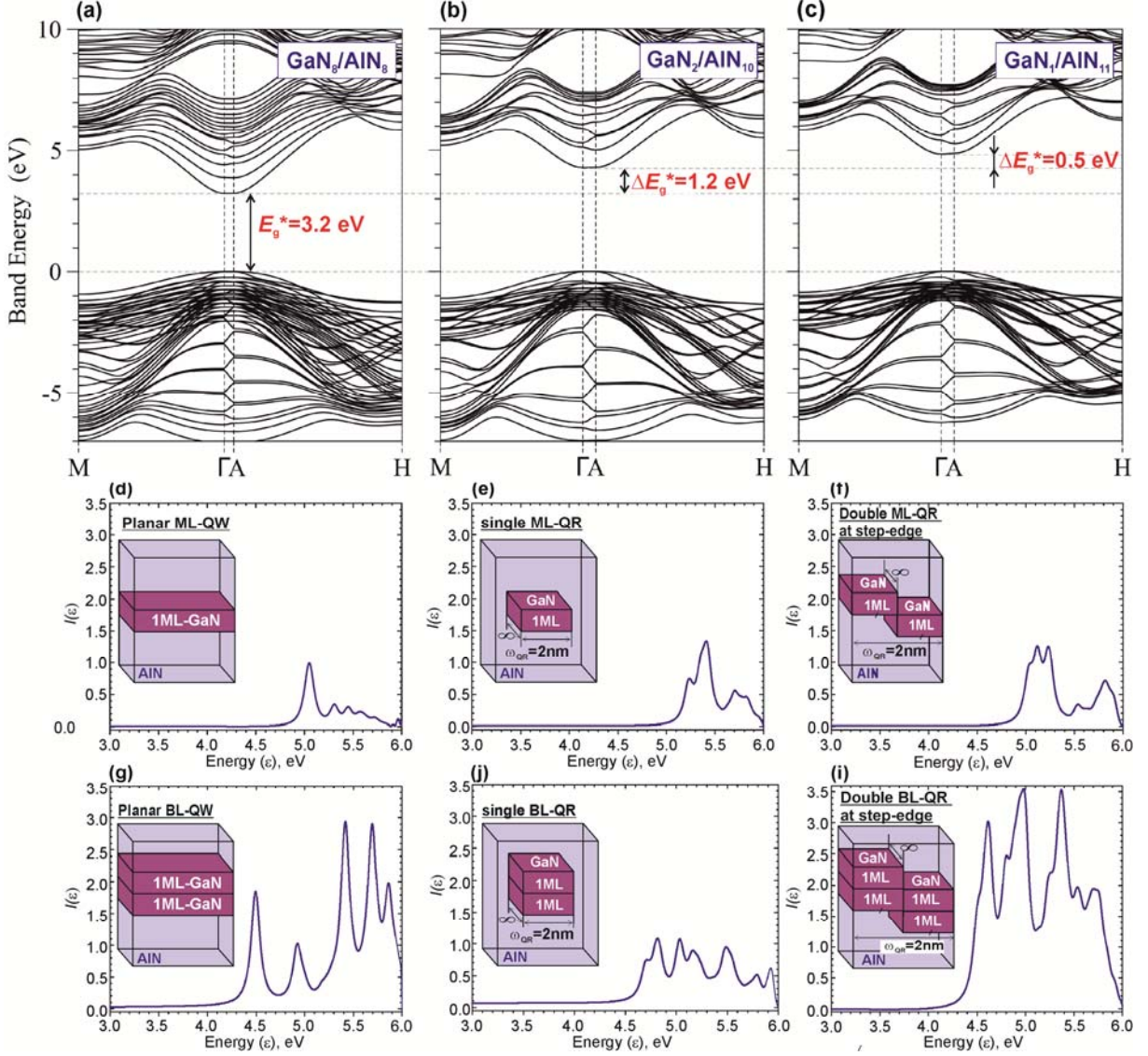


Figure 3. Electronic band structures of the symmetric GaN₈/AlN₈ superlattice (a), MQW structures GaN₂/AlN₁₀ (b), and GaN₁/AlN₁₁ (c), calculated using the G₀W₀ method. (d-i) Spectra of optical transitions in GaN_m/AlN₁₀ ($m=1,2$) heterostructures with different configurations of GaN atomic layers shown (not to scale) in the insets of each figure. The graphs also show the calculated values of E_g^* and intensities of optical transitions.

TABLE 2. Characteristics of quantum-dimensional GaN/AlN structures, determined from their spectra of optical transitions

	Planar QWs		Single QRs in AlN matrix		Double QRs adjacent to step-edge	
	$E_g^*(\text{eV})$	I	$E_g^*(\text{eV})$	I	$E_g^*(\text{eV})$	I
1ML	4.929	0.99	5.120	1.35	4.912	1.27
2ML	4.381	1.86	4.577	1.09	4.387	3.02

Figure 3d–i show the spectra of optical transitions in the most interesting optical range of 3–6 eV, calculated by the DFT method using supercell approach for various configurations of GaN/AlN QWs with both ML and BL thicknesses. In addition to calculating the spectra of

infinite planar QWs of different thicknesses (Figure 3d and g), we also calculated the spectra for so-called QRs with the same width of 2 nm (limited by the computational resources used) in one direction and an infinite size in the other direction. For each QR's thickness, two configurations were analyzed: single QRs in a homogeneous AlN matrix (Figure 3e and j) and double QRs adjacent at the step edges (Figures 3f and i). The E_g^* values for these structures were determined from the coordinate of the intersection of the tangent to the low-energy edge of the spectrum with the energy axis. To quantitatively characterize the brightness of the emission from the structures, the intensities of optical transitions ($I(E)$) were calculated using the general equation:^[82]

$$I(E) = \sum \sum \int \frac{dk}{(2\pi)^3} F_{ij}(k) \delta(E_{ik} - E_{jk} - E), \quad (1)$$

where i and j are indices of occupied bands, respectively, and momentum matrix elements F_{ij} are calculated for a given direction \hat{u} using equation:

$$F_{ij} = |\langle \psi_{ik} | \hat{u}r | \psi_{jk} \rangle| \quad (2)$$

The E_g^* and I values determined by DFT-sumualtion for all structures shown in Figure 3d-i are summarized in Table 2. The data for the infinite planar ML- and BL-thick QWs, in addition to confirming a significant difference between their E_g^* of approximately 0.5 eV, showed a significantly higher intensity of optical transitions (absorption and emission) for the latter with the lowest value of E_g^* value.

This analysis reveals the quantum confinement effect in QRs of both thicknesses, namely, an increase in E_g^* by approximately 200 meV compared to planar QWs. Regarding the $I(E)$ of the QRs, only a small increase is observed for single ML-thick QRs, while for BL-thick QRs, its magnitude is even smaller than for an infinite planar BL-QW. However, both double QRs adjacent to the step edges exhibit a significant increase in $I(E)$, and this effect is especially pronounced for BL-thick QRs (Figure 3i).

5. Optical Properties of fractional monolayer GaN/AlN quantum wells

5.1 Photoluminescence spectra

Figure 4a and S10 show the PL spectra of the T -series structures, which demonstrate a redshift in the position of the main single PL peak by approximately 600 meV with a gradual increase in the m from 0.75 to 2 ML in 0.25 ML increments. Since this shift is almost consistent with the results of theoretical calculations of the electronic structure of ML and BL QWs presented in Figure 3a, the upper and lower PL energy limits of 5.45 and 4.81 eV in Figure 4d are denoted by the symbols Λ_{ML} and Λ_{BL} .

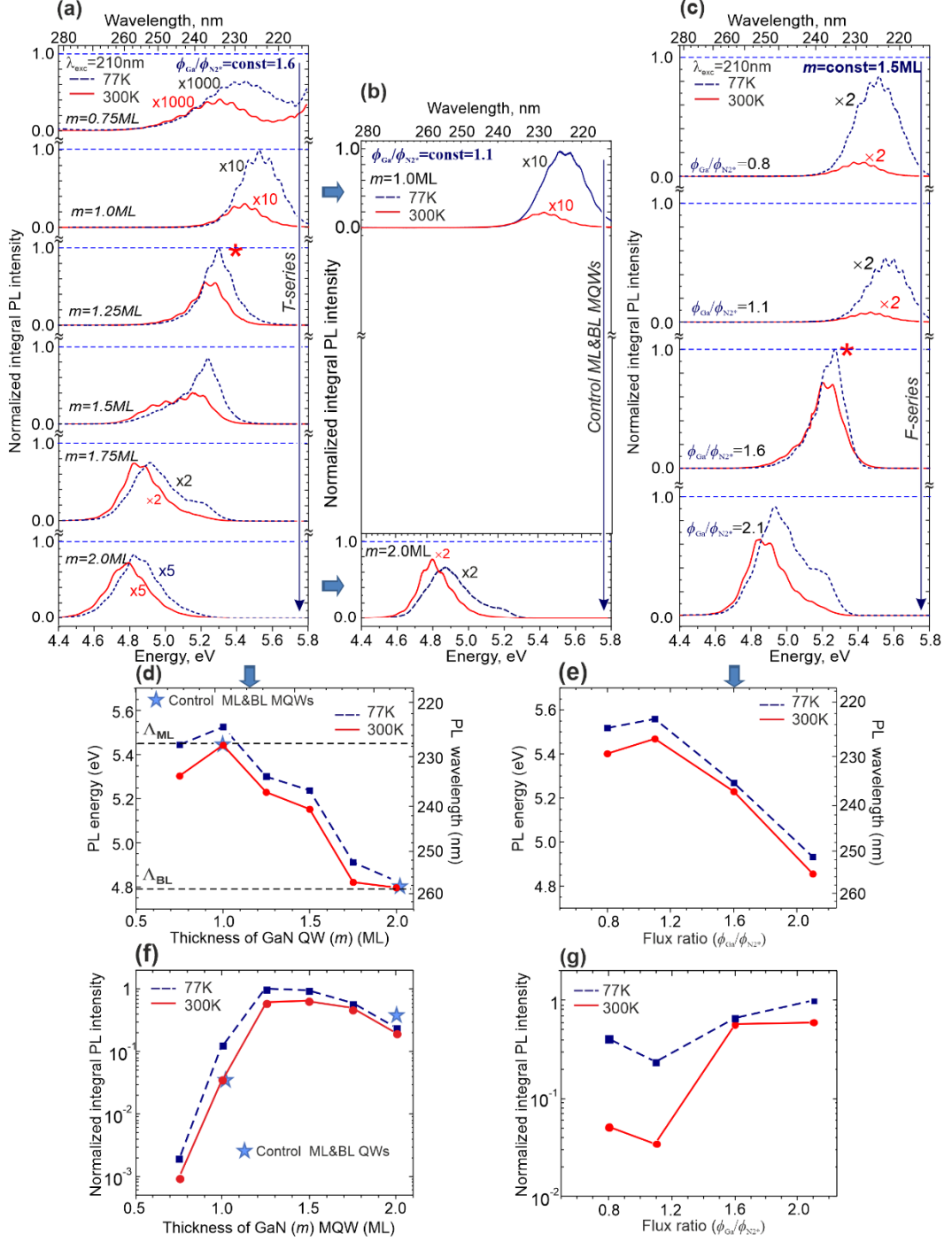


Figure 4. PL spectra (77&300K) of $250 \times \{\text{GaN}_m/\text{AlN}_{15}\}$ MQW structures with $m=0.75-2$ ML and $\phi_{\text{Ga}}/\phi_{\text{N}2^*}=1.6$ (T-series) (a) and two control structures with $m=1$ and 2 ML grown at $\phi_{\text{Ga}}/\phi_{\text{N}2^*}=1.1$ (b). All PL intensities are normalized relative to the maximum PL peak intensity observed at 77K in the structure marked with a star in (a). (b). (c) PL spectra (77&300K) of $250 \times \{\text{GaN}_{1.5}/\text{AlN}_{16}\}$ MQW structures grown with $\phi_{\text{Ga}}/\phi_{\text{N}2^*} = 0.8-2.1$ (F-series). (d) and (e) Dependencies of PL energy (77&300K) on QW thickness in T-series and $\phi_{\text{Ga}}/\phi_{\text{N}2^*}$ in F-series, respectively. (f) and (g) Dependencies of normalized PL intensities (77&300K) on QW thickness in T-series and $\phi_{\text{Ga}}/\phi_{\text{N}2^*}$ in F-series, respectively.

It is important to note that the spectral position, shape and integrated intensity of the two PL spectra of the MQW structures in the *T*-series grown with an integer $m = 1$ and 2 at $\phi_{\text{Ga}}/\phi_{\text{N}2^*} = 1.6$ show almost complete agreement with the characteristics of the PL spectra in Figure 4b, obtained for the control MQW structures grown with the same m , but at a lower value of $\phi_{\text{Ga}}/\phi_{\text{N}2^*} = 1.1$ (see also Figure 4d and f). In contrast, Figure 4c shows the PL spectra of the *F*-series structures with the same fractional value of $m = 1.5$, whose luminescence characteristics clearly depend on the $\phi_{\text{Ga}}/\phi_{\text{N}2^*}$, which in this series varied from 0.8 to 2.1. An analysis of these spectral features will be presented in Section 6.

5.2 Cathodoluminescence spectra

The spectral positions and relative intensities of the main peaks in the CL spectra of both series of MQW structures are similar to those in the PL spectra of the same structures. This conclusion is valid for the CL spectra excited using both high- and low-current electron (*e*-) guns, which are shown in **Figure 5(a)** and S11, respectively.

The upper oscillogram in Figure 5(b) shows the temporal changes in the output UVC radiation emitted by the *F-1.6* structure when it is pumped by the high-current pulsed *e*-beam shown in the lower oscillogram.^[83] Although each *e*-beam current pulse and, accordingly, the output UVC-radiation pulse have unique shapes, their integral characteristics are quite reproducible. Using these and other oscillograms for all *F*-series structures, the dependencies of the peak output UVC optical power (P) on the *e*-beam pump current (I_e) were plotted in Figure 5c and d). All MQW structures exhibit linear $P(I_e)$ curves, and the maximum peak power of $P_{\text{max}} = 37$ W at a pump current of 1.8 A was observed in the *F-2.1* structure (Figure 5c), which emits at the longest wavelength in this series, 256 nm. It is worth noting that this same structure demonstrated the highest integrated PL intensity at the same wavelength (Figure 4c and g). The structures grown at the N-rich conditions *F-0.8* and *F-1.1* demonstrated much less $P_{\text{max}} = 1\text{--}3$ W, as shown in Figure 5d.

In the *T*-series, the maximum value of P $P_{\text{max}} \approx 21$ W at a pump current of 1.8 A was observed in samples with the thickest m , *T-1.75ML* and *T-2.0ML* (Figure S12), which also emitted in the relatively long-wavelength range of 257–267 nm. Structures in this series with thinner wells, *T-0.75* and *T-1.0*, emitted at shorter wavelengths ~ 230 nm, exhibited significantly lower P_{max} of about 1 W.

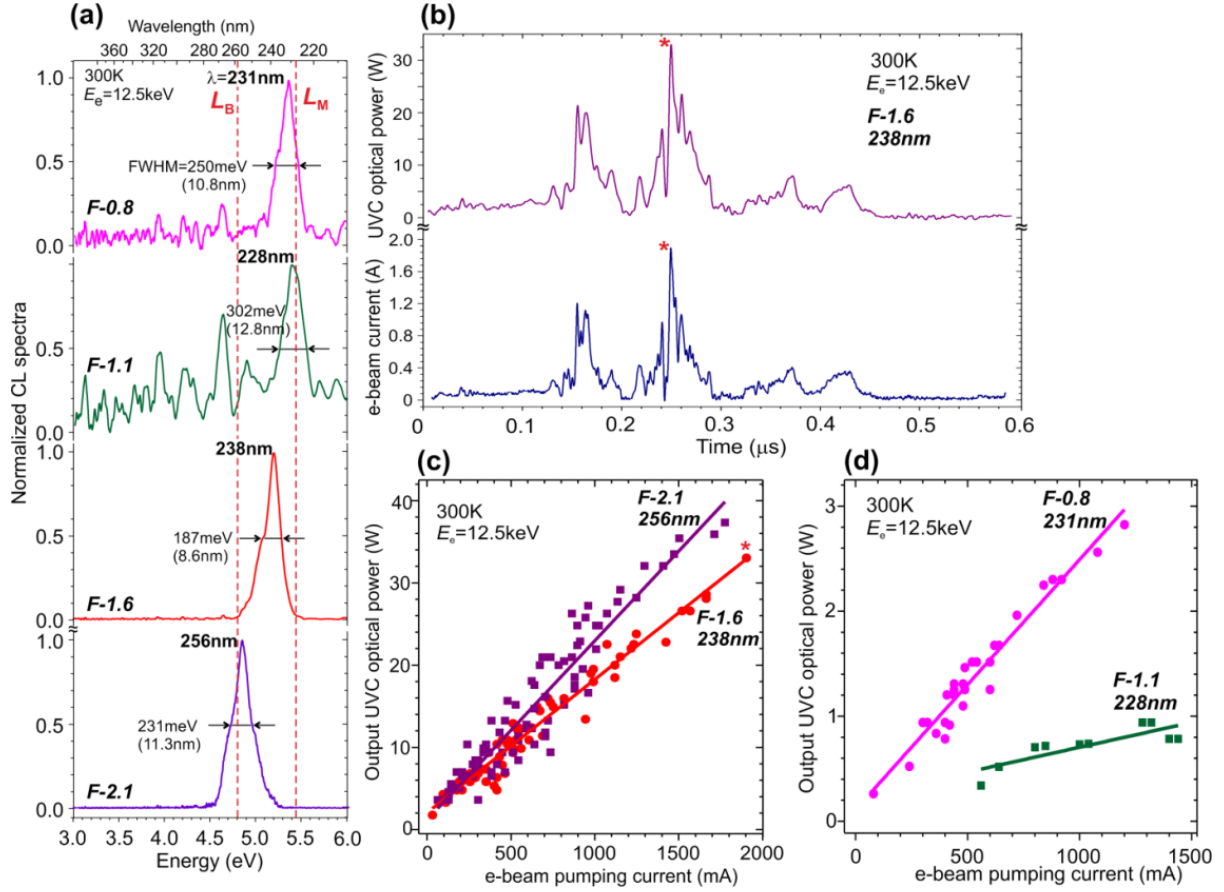


Figure 5. (a) CL spectra (300K) of the *F*-series structures excited by a high-current *e*-gun. (b) Oscillograms showing simultaneous changes in the output UVC-optical power from the *F*-1.6 structure (upper curve) and the pumping pulsed *e*-current ($E_e=12.5\text{ keV}$, I_e up to 1.9 A) (lower curve). Current dependences of the peak optical output powers ($P(I_e)$) of the *F*-series structures: *F*-2.1, *F*-1.6 (c) and *F*-1.1, *F*-0.8 (d). The experimental data for the *F*-1.6 structure, marked with an asterisk in (b) correspond to the same asterisk in the $P(I_e)$ dependence in (c).

Of more interest and practical significance are the results obtained for the *F*-1.6 and *T*-1.25ML structures grown at the moderate Ga-rich conditions with $m=1.25\text{-}1.5$ ML. The former structure not only emits a single narrow CL peak at 238 nm with a half-width of 187 meV (8.6 nm) but also ensures a $P_{\max}=33\text{ W}$ at $I_e=1.9\text{ A}$, which is more than three times higher than our best result for an *e*-beam pumped UVC-emitter at the same wavelength, demonstrated in our previous work.^[50] Moreover, this structure exhibits an optical energy per pulse of up to 2.6 μJ , as shown in Figure S13. The *T*-1.25ML structure emitted at almost the same wavelength of 237 nm, but its maximum power was approximately half as high (Figure S12).

6. Discussion: phenomenological model of growth and optical properties of fractional GaN/AlN MQWs

The optical properties of GaN/AlN MQW structures with nominal integer and fractional QW thicknesses in the subcritical range ($m \leq 2$), described in Section 5, can be explained using the following phenomenological growth model based on theoretical calculations of the electronic structures of various configurations 2D-GaN objects in AlN matrix (Section 4), as well as using the results of experimental studies of the PA MBE growth kinetics (Section 2) and structural properties (Section 3) of such structures.

It can be assumed that the emission spectra of the studied GaN/AlN MQW structures are determined by the thickness and topology of the QWs. In Section 2, we established the influence of $\phi_{\text{Ga}}/\phi_{\text{N}2^*}$ on the dominance of either the 2D-growth nucleation or the step-flow growth mechanism during the formation of GaN QWs (Fig. 1). Therefore, the similarity of the PL spectra of the structures grown with the same integer $m = 1$ and 2 , but under different conditions ($\phi_{\text{Ga}}/\phi_{\text{N}2^*} = 1.1$ and 1.6), observed in Figure 4a and b, indicates their layer-by-layer growth and the independence of the optical properties of GaN 2D-QWs from the specific filling mechanisms of the lower and upper layers in structures with $m < 2$.

When analyzing the T -series structures with $m = 1$, we assume a continuous topology of ML-thick QWs, while QWs with $m < 1$ have a discontinuous topology. The extremely low PL intensities in these structures can be explained by the relatively low intensities of optical transition in 1ML thick QWs, as shown in Table 2. In addition, the relatively low quantum efficiency of the these QWs, estimated from the relatively low ratio of PL peak intensities at high and low-temperatures, can be explained by the absence of thickness and composition fluctuations in these QWs, which usually enhance this ratio due to formation of potential relief in the QWs. The relatively low CL intensity for these structures with extremely thin (1 ML) QWs may also be due to the low efficiency of capture of charge carriers diffusing from the barrier layers, which was recently demonstrated by us.^[84] Thus, both the calculated higher values of the optical transition intensities and the expected higher carrier capture efficiencies in BL-thick quantum-dimensional objects formed in QWs with a nominal fractional thickness of $1 < m \leq 2$ enhanced our attention to these astructures analyzed below.

According to Section 2, the step-flow growth mechanism plays a central role in the growth of QWs in all structures in the T -series with $m > 1$ under identical Ga-enriched conditions $\phi_{\text{Ga}}/\phi_{\text{N}2^*} = 1.6$. Consequently, the change in the second ML coverage (θ_2) from 0.25 to 1 with a corresponding increase in m from 1.25 to 2 ML occurs as a parallel movement of the step edges, leading to a sequential broadening of the BL-thick QRs, as

shown in Figure 1d and S14. Therefore, one can estimate the upper limit of the QR's width $\omega_{QR} = \omega_T \theta_2$ using the data of AFM measurements in Figure 2a. It should be noted that for the *T*-1.25 structure, which exhibits a relatively high integrated PL intensity in the short-wavelength emission range of 230–240 nm, this estimate yields $\omega_{QR} \sim 10$ nm. However, in reality, QRs are likely to have a more complex non-rectangular topology due to the anisotropy of the growth rate in different crystallographic directions.^[85] Furthermore, ω_{QR} can be reduced due to the parasitic 2D nucleation growth mechanism leading to the formation of GaN 2D-QDs instead of the expansion of 2D-QRs.

In the *F*-series structures, the use of different values of ϕ_{Ga}/ϕ_{N2*} at a constant $m = 1.5\text{ML}$ ($\theta_2 = 0.5$) suggests a strong dependence of the topology of the second upper layer of GaN QW on the growth conditions. At small values of $\phi_{Ga}/\phi_{N2*} = 0.8–1.1$, the dominance of the 2D-nucleation growth mechanism described in Section 2 should result in the formation of individual BL-thick QDs during the growth of the upper ML. Importantly, that these QDs not only emit in the most demanded spectral range of 220–230 nm, but also have a significantly higher emission intensity compared to the emission in the same spectral range observed for GaN ML-thick 2D-objects in *T*-0.8 and *T*-1.0 structures, respectively, analyzed above.

The significant and threshold increase in the UVC-radiation intensity by more than an order of magnitude is achieved in GaN QWs grown under Ga enriched conditions ($\phi_{Ga}/\phi_{N2*} \geq 1.6$), emitting in the range >230 nm. Since these conditions lead to an increase in the role of the step-flow growth mechanism, this increase in the emission intensity can be presumably explained by the formation of QR-like objects near the step edges, as described in Section 2. This phenomenon is most interestingly manifested in the *F*-1.6 and *T*-1.25ML structures (Figure 4a and c) with the expected high concentration of QRs with a relatively narrow nominal width of <10 nm, which apparently leads to relatively bright emission in the sub-240 nm range. The observed redshift of emission to the spectral region of 250 – 260 nm in structures from both series *F*-2.1, *T*-1.5, *T*-1.75, *T*-2 with expected wider QRs, leading to a decrease in quantum confinement in them, further confirms this hypothesis.

Of course, the qualitative model developed above is overly simplified, since, as discussed in Section 2, under nonequilibrium PA MBE conditions, a mixed GaN growth mode is assumed, with the simultaneous formation of GaN 2D-QRs and 2D-QDs of varying sizes and locations on an AlN ML-stepped surface. Therefore, future research is needed to study the dependence of the characteristics of all possible 2D-GaN objects in the fractional ML GaN/AlN MQW structures on growth conditions, nominal thicknesses, and the imperfections of buffer layers, among other factors.

7. Conclusion

In summary, we investigate the capabilities of PA MBE for the growth of *e*-beam pumped powerful UVC-emitters based on $250 \times \{\text{GaN}_m/\text{AlN}_{15}\}/\text{AlN}/c\text{-Al}_2\text{O}_3$ MQW structures with nominal subcritical QW thicknesses $m = (0.75-2) \pm 0.25\text{ML}$ grown at various $\phi_{\text{Ga}}/\phi_{\text{N}2^*} = 0.8-2.1$. RHEED studies show that the growth of such QWs on AlN barrier layers with a atomically smooth ML-stepped topography occurs with the dominance of either a 2D-nucleation growth mechanism under nitrogen-rich and unit stoichiometry conditions ($\phi_{\text{Ga}}/\phi_{\text{N}2^*} \leq 1$) or a step-flow growth mechanism under Ga-rich conditions ($\phi_{\text{Ga}}/\phi_{\text{N}2^*} \geq 1.6$).

Based on experimental studies and theoretical calculations, a phenomenological model for the formation of $\{\text{2D-GaN}_m/\text{AlN}\}$ MQW structures in the subcritical region $m \leq 2$ is proposed. In this model, the observed independence of the emission spectral characteristics of MQWs with integer $m = 1,2$ on the growth conditions ($\phi_{\text{Ga}}/\phi_{\text{N}2^*}$) is explained by the layer-by-layer growth of these wells with a continuous topology, independent of their growth mechanism. The PL and CL spectra of these MQW structures with $m = 1$ and 2 MLs exhibit single peaks at 5.45 and 4.81 eV, respectively, which is consistent with ab initio G_0W_0 calculations of their electronic structures. The emission at 256 nm from BL-thick QWs is significantly more intense than the short-wavelength emission at 228 nm from ML-thick QWs. This difference can be explained by two factors, both of which increase in thicker BL-thick QW and associated quantum-dimensional objects QRs and QDs. First, this is the intensities of optical transitions, and in the context of CL, this factor is supplemented by more efficient carrier capture. The variability of the spectral position and integrated intensity of the luminescence peaks of fractional-thickness QWs is explained by the formation of different 2D-GaN objects depending on the nominal well thickness and growth conditions. It is assumed that the dominance of the 2D-nucleation growth mechanism during the growth of GaN QWs under nitrogen-rich and unit stoichiometrical conditions leads to the formation of individual 2D-GaN QDs with M- ($m < 1$) or BL- ($m > 1$) thicknesses. In both cases, relatively weak emission is observed in the $220-230$ nm range, but at $m > 1$ its intensity is higher. Upon transition to moderately Ga-enriched conditions ($\phi_{\text{Ga}}/\phi_{\text{N}2^*} \sim 1.6$), a sharp increase in the emission intensity is observed in the $230-240$ nm range in a narrow range of $m = (1.25-1.5)$ ML, which is associated with an increasing role of the stepflow growth mode of GaN, leading to the formation of narrow (<10 nm) 2D QRs elongated along the step edges. The observed broadening and redshift of the luminescence peaks to the region of $(250-260)$ nm with a further increase in $\phi_{\text{Ga}}/\phi_{\text{N}2^*}$ to 2.1 and m to 1.75 is probably associated with the lateral

broadening of BL-thick 2D QRs and QDs BL formed in a mixed growth mode, combining the mechanisms of 2D nucleation and step-flow growth modes.

Measurements of the CL spectra of MQW structures excited using different *e*-guns with output *e*-beam currents from 1 mA to 2 A and energies up to 12.5 keV not only confirm the above-described growth model, but also demonstrate a possibility of generation of UVC radiation with single peaks in the wavelength range from 228 to 256 nm and maximum peak output optical powers from 1 to 37 W, respectively, linearly increasing with increasing *e*-beam current up to 2 A. It should be emphasized that MQW structures with fractional ML-thick QWs in the form of BL-thick 2D-QRs with $\omega_{QR} < 10$ nm exhibit a single CL peak at 238 nm with a half-width of 8.6 nm and an optical power linearly varying to 33 W with an increase of pumping *e*-current to 1.9 A. The optical energy of this UVC-radiation is 2.6 μ J per pulse with a duration of 0.5 μ s.

Experimental Section/Methods

A. Experiment

All samples were fabricated by PA MBE (Compact 21T, Riber) on 2-inch *c*-Al₂O₃ substrates on which AlN nucleation and buffer layers with a total thickness of ~ 1.5 μ m were grown using sequential migration-enhanced epitaxy and three-step metal-modulated epitaxy in the temperature range of 790-850°C, as described in Refs. 86,87. The growth of active regions with $250 \times \{\text{GaN}_m/\text{AlN}_n\}$ ($m=0.75-2$ ML, $n=15$ ML) MQWs was described in detail in our previous paper.[49,50] Briefly, all structures were grown at the same substrate temperature of 690°C and ϕ_{N2^*} of 0.55 ± 0.004 ML/s, which was used to control the nominal thicknesses of m and n , most of which were grown under metal-rich conditions. In one sample with QWs grown under nitrogen-rich conditions, a ϕ_{Ga} was used to control m . AlN barrier layers were grown under slightly Al-enriched conditions with an flux ratio of $\phi_{\text{Al}}/\phi_{N2^*}=1.1$ and using BL-thick Al pre-deposited before the growth of each AlN. Also, before the growth of each QW, the AlN surface was exposed to an ϕ_{N2^*} to consume excess Al. Two series of samples were grown. In the *F*-series, the flux ratio $\phi_{\text{Ga}}/\phi_{N2^*}$ was varied from 0.8 to 2.1 by changing the ϕ_{Ga} at a constant $m=1.5$ ML. In the *T*-series, the value of m was varied from 0.75 to 2 ML with a step of 0.25 ML at a constant $\phi_{\text{Ga}}/\phi_{N2^*}=1.6$. To designate the samples, the series symbols *F*- or *T*- were followed by numerical values of $\phi_{\text{Ga}}/\phi_{N2^*}$ or m , respectively. In addition, two control $250 \times \{\text{GaN}_m/\text{AlN}_{15}\}$ MQW structures with integer $m=1$ and 2 ML were grown at $\phi_{\text{Ga}}/\phi_{N2^*}=1.1$. All MQW structures were terminated with a 15-ML-thick AlN top layer.

All growth stages were monitored *in situ* using reflection high-energy electron diffraction (RHEED), laser interferometry and multi-beam optical stress sensor. Atomic force and scanning electron microscopes (AFM and SEM, respectively), X-ray diffraction (XRD) and small-angle X-ray reflection (XRR) curve measurements using D8DISCOVER, Bruker AXS diffractometer with a rotation anode (CuK α 1 radiation) were used for post-growth studies of the structural properties of the MQW structures. High-angle annular dark-field scanning transmission electron microscopy (HAADF-STEM) images were recorded using a spherical aberration-corrected FEI Titan Cubed Themis G2 300 transmission electron microscope (TEM) operated at 300 kV. The TEM samples were prepared by mechanical polishing and argon ion milling using Gatan PIPS™ Model 691.

PL was excited by the radiation of a fourth-harmonic generator (Coherent) pumped by a Topol-1050-C-NC parametric femtosecond laser (Femtonika LLC) produced 80 MHz pulses with a duration of 150 fs. The excitation wavelength and average power density were 210 nm and ~ 0.03 W/cm 2 , respectively. The PL spectra, acquired at either 77 K or RT, were recorded using an Acton SP2500 spectrometer (Princeton Instruments) equipped with an 1800 grooves/mm diffraction grating and a liquid-nitrogen-cooled CCD camera (Pylon, Princeton Instruments).

The CL spectra were excited using both low- and high-current electron (*e*-beams) guns, which were recently reviewed in Ref.83. In the former, the *e*-beam with the energy $E_e=10$ keV was emitted by a standard incandescent electron gun (*e*-gun) with a tungsten cathode with the maximum value of the *cw*-electron current $I_e=1$ mA and the *e*-beam diameter on the sample surface $D_e=1$ mm. To generate high-current *e*-beams with $D_e=4$ mm, a pulsed *e*-gun based on a high-voltage surface discharge over a ferroelectric was used to provide the generation of *e*-current pulse packets with a total duration and frequency of ~ 0.5 μ s and 12 Hz, respectively. The high-current *e*-beam had $E_e\sim 12.5$ keV and the amplitudes of its current varied randomly during the discharge pulse up to 2 A. The *e*-beam current and CL spectra were registered using a miniature spectrograph with a concave diffraction grating, in which the signal was recorded on a CCD array with signal accumulation (see Section SII in Supplementary).

B. Theory

The *ab initio* calculations of optical spectra of GaN_{*m*}/AlN₁₀ (*m* = 1,2) heterostructures were carried out within local density approximation (LDA) to the density functional theory (DFT) using the pseudopotential method and the plane-wave basis set for wavefunctions as implemented in ABINIT software package.^[88,89] The 2s2p, 3s3p, and 3d4s4p electronic states

were considered as valence for Al, N and Ga atoms respectively. The expansion of wave functions on a plane-wave basis was controlled by completeness of the basis which determined by the cutoff energy $E_{\text{cut}}=40$ Ha. The reciprocal space sampling was performed on an $8\times 8\times 6$ and $4\times 4\times 1$ grid for bulk crystals and heterostructures correspondingly using the Monkhorst-Pack scheme.^[90] The structural parameters were optimized for all structures until forces on atoms become less than 10^{-4} Ha/bohr and total stress below 0.1 GPa. The calculations of electronic structure were held with 150 unoccupied bands taken into account.

The calculations of electronic structure of limited set of ideal QW heterostructures $(\text{GaN})_8/(\text{AlN})_8$, $(\text{GaN})_2/(\text{AlN})_{10}$ and $(\text{GaN})_1/(\text{AlN})_{11}$ were additionally carried out using single shot G_0W_0 quasiparticle approximation.^[91,92] The quasiparticle energies were calculated using Kohn–Sham eigenstates and eigenvalues as an initial solution of non-interacting Hamiltonian. The inverse dielectric matrix was calculated using random phase approximation (RPA). The corrections to Kohn–Sham energies were calculated as $[\Sigma-E_{\text{xc}}]$ operator diagonal matrix elements, where $\Sigma=i\text{GW}$ —self-energy operator, E_{xc} – exchange-correlation energy operator, G – Green function, and W – screening Coulomb interaction operator. The components of wavefunction with energies below 35 Ha for both exchange and correlation part were used to calculate Σ . The set of QW configurations structures with structural distortions were constructed using supercell approach.

Supporting Information

Supporting Information is available from the Wiley Online Library or from the author.

Acknowledgements

This work was supported by National Key R&D Program: Intergovernmental International Science and Technology Innovation Cooperation, Project №2022YFE0140100

Conflict of Interest

The authors declare no conflict of interest.

Author Contributions

Data Availability Statement

The data that support the findings of this study are available in the supplementary material of this article.

Received: ((will be filled in by the editorial staff))

Revised: ((will be filled in by the editorial staff))

Published online: ((will be filled in by the editorial staff))

References

1. R. Dingle, W. Wiegmann, C. H. Henry, "Quantum states of confined carriers in very thin $\text{Al}_x\text{Ga}_{1-x}\text{As}$ - $\text{GaAs}-\text{Al}_x\text{Ga}_{1-x}\text{As}$ heterostructures", *Phys. Rev. Lett.* 33, (1974): 827. <https://doi.org/10.1103/PhysRevLett.33.827>
2. R. D. Dupius, P. D. Dapkus, N. Holonyak, Jr., E. A. Rezek, R. Chin, "Room-temperature laser operation of quantum-well $\text{Ga}_{(1-x)}\text{Al}_x\text{As}$ - GaAs laser diodes grown by metalorganic chemical vapor deposition", *Appl. Phys. Lett.* 32, (1978): 295. <https://doi.org/10.1063/1.90026>
3. A. I. Ekimov, A. A. Onushchenko, "Quantum size effect in three-dimensional microscopic semiconductor crystals," *JETP Lett.* 34, (1978): 345. <https://doi.org/10.1134/S0021364023130040>
4. Y. Arakawa, H. Sakaki, "Multidimensional quantum well laser and temperature dependence of its threshold current," *Appl. Phys. Lett.* 40, (1982): 939. <http://dx.doi.org/10.1063/1.92959>
5. E. Bauer, "Phänomenologische Theorie der Kristallabscheidung an Oberflächen. I," *Zeitschrift für Kristallographie* 110 (1–6), (1958): 372. <http://dx.doi.org/10.1524/zkri.1958.110.1-6.372>
6. I. N. Stranski, L. Krastanow, (1938). "Zur Theorie der orientierten Ausscheidung von Ionenkristallen aufeinander". Abhandlungen der Mathematisch-Naturwissenschaftlichen Klasse IIb. Akademie der Wissenschaften Wien. 146: 797. <http://dx.doi.org/10.1007/BF01798103>
7. B. Daudin, F. Widmann, G. Feuillet, Y. Samson, M. Arlery, and J. L. Rouvie`re, "Stranski-Krastanow growth mode during the molecular beam epitaxy of highly strained GaN ", *Phys. Rev. B* 56, no. 12, (1997): R7069. <https://doi.org/10.1103/PhysRevB.56.R7069>
8. F. Widmann, J. Simon, B. Daudin, G. Feuillet, J. L. Rouvie`re, and N. T. Pelekanos, G. Fishman, "Blue-light emission from GaN self-assembled quantum dots due to giant piezoelectric effect", *Phys. Rev. B* 58(24), (1998): R15 989. <https://doi.org/10.1103/PhysRevB.58.R15989>
9. C. Adelmann, J. Brault, J.-L. Rouvie`re, H. Mariette, Guido Mula, and B. Daudin, "Atomic-layer epitaxy of GaN quantum wells and quantum dots on (0001) AlN ", *J. Appl. Phys.* 91, no. 8, (2002): 5498. <https://doi.org/10.1063/1.1458049>
10. C. Adelmann, B. Daudin, R. A. Oliver, G. A. D. Briggs, R. E. Rudd, "Nucleation and growth of GaN/AlN quantum dots", *Phys. Rev. B* 70, (2004): 125427. <https://doi.org/10.1103/PhysRevB.70.125427>
11. J. Brown, F. Wu, P. M. Petroff, and J. S. Speck, "GaN quantum dot density control by rf-plasma molecular beam epitaxy", *Appl. Phys. Lett.* 84, (2004): 690. <http://dx.doi.org/10.1063/1.1645333>
12. O. Brandt, T. Flissikowski, D. M. Schadt, U. Jahn, A. Trampert, and H. T. Grahn, "Long-time evolution of the photoluminescence in C - and M -plane GaN/AlN quantum dots upon intense ultraviolet irradiation," *Appl. Phys. Lett.* 93, (2008): 081907. <http://dx.doi.org/10.1063/1.2973404>
13. G. Koblmüller, R. Averbeck, H. Riechert, Y.-J. Hyun, P. Pongratz, "Strain relaxation dependent island nucleation rates during the Stranski-Krastanow growth of GaN on AlN by molecular beam epitaxy," *Appl. Phys. Lett.* 93, (2008): 243105. <http://dx.doi.org/10.1063/1.3046730>
14. L. Lahourcade, S. Valdueza-Felip, T. Kehagias, G. P. Dimitrakopoulos, P. Komninou, and E. Monroy, "Stranski-Krastanow growth of (112̄2)-oriented GaN/AlN quantum dots," *Appl. Phys. Lett.* 94, (2009): 111901. <http://doi.org/10.1063/1.3095499>
15. Z. Gac̄evic̄, A. Das, J. Teubert, Y. Kotsar, P. K. Kandaswamy, Th. Kehagias, T. Koukoula, Ph. Komninou, and E. Monroy, "Internal quantum efficiency of III-nitride quantum dot

superlattices grown by plasma-assisted molecular-beam epitaxy“, *J. Appl. Phys.* 109, (2011): 103501. <https://doi.org/10.1063/1.3590151>

16. C. Himwas, R. Songmuang, Le Si Dang, J. Bleuse, L. Rapenne, E. Sarigiannidou, E. Monroy “Thermal stability of the deep ultraviolet emission from AlGaN/AlN Stranski-Krastanov quantum dots“, *Appl. Phys. Lett.* 101, (2012): 241914. <http://dx.doi.org/10.1063/1.4770075>

17. B. Damilano, N. Grandjean, F. Semond, J. Massies, and M. Leroux, “From visible to white light emission by GaN quantum dots on Si (111) substrate,“ *Appl. Phys. Lett.* 75, (1999): 962. <http://dx.doi.org/10.1063/1.124567>

18. S. Tamariz, G. Callsen, and N. Grandjean, “Density control of GaN quantum dots on AlN single crystal,“ *Appl. Phys. Lett.* 114, (2019): 082101. <http://dx.doi.org/10.1063/1.5083018>

19. M. Miyamura, K. Tachibana, and Y. Arakawa, “High-density and size-controlled GaN self-assembled quantum dots grown by metalorganic chemical vapor deposition,“ *Appl. Phys. Lett.* 80, (2002): 3937. <https://dx.doi.org/10.1063/1.1482416>

20. J. C. Zhang, B. Meyler, A. Vardi, G. Bahir, J. Salzman, “Stranski-Krastanov growth of GaN quantum dots on AlN template by metalorganic chemical vapor deposition,“ *J. Appl. Phys.* 104, (2008): 044307. <http://dx.doi.org/10.1063/1.2969915>

21. T. Maruyamaa, H. Otsuboa, T. Kondo, Y. Yamamoto, S. Naritsuka, “Fabrication of GaN dot structure by droplet epitaxy using NH₃,“ *J. Cryst. Growth* 301-302, (2007): 486. <http://dx.doi.org/10.1016/j.jcrysGro.2006.09.031>

22. K. Bellmann, F. Tabataba-Vakili, T. Wernicke, A. Strittmatter, G. Callsen, A. Hoffmann, M. Kneissl, “Desorption induced GaN quantum dots on (0001) AlN by MOVPE,“ *Phys. Status Solidi RRL* 9, no. 9, (2015): 526. <https://doi.org/10.1002/pssr.201510217>

23. F. Bernardini, V. Fiorentini, and D. Vanderbilt, “Spontaneous polarization and piezoelectric constants of III-V nitrides,“ *Phys. Rev. B* 56, (1997): R10 024. <https://doi.org/10.1103/PhysRevB.56.R10024>

24. K. S. Novoselov, A. K. Geim, S. V. Morozov, D. Jiang, Y. Zhang, S. V. Dubonos, I. V. Grigorieva, A. A. Firsov, “Electric Field Effect in Atomically Thin Carbon Films,“ *Science* 22 October, V. 306, (2004): 666. <https://doi.org/10.1126/science.1102896>

25. H. Chang, Z. Chen, W. Li, J. Yan, R. Hou, S. Yang, Z. Liu, G. Yuan, J. Wang, J. Li, P. Gao, T. Wei, “Graphene-assisted quasi-van der Waals epitaxy of AlN film for ultraviolet light emitting diodes on nano-patterned sapphire substrate,“ *Appl. Phys. Lett.* 114, (2019): 091107. <https://doi.org/10.1063/1.5081112>

26. Z. Cheng, R. Cao, K. Wei, Y. Yao, X. Liu, J. Kang, J. Dong, Z. Shi, X. Li, X. Zhang, “2D Materials Enabled Next-Generation Integrated Optoelectronics: from Fabrication to Applications,“ *Adv. Sci.*, 8, (2021): 2003834. <https://doi.org/10.1002/advs.202003834>

27. J. Ben, X. Liu, C. Wang, Y. Zhang, Z. Shi, Y. Jia, S. Zhang, H. Zhang, W. Yu, D. Li, X. Sun, “2D III-Nitride Materials: Properties, Growth, and Applications,“ *Adv. Mater.* 33, (2021): 2006761. <https://doi.org/10.1002/adma.202006761>

28. M. Fujita, K. Wakabayashi, K. Nakada, K. Kusakabe, “Peculiar localized state at zigzag graphite edge,“ *J. Phys. Soc. Jpn.* 65, no. 7, (1996):1920. <https://doi.org/10.1143/JPSJ.65.1920>

29. P. V. Shinde, A. Tripathi, R. Thapa, C. Sekhar Rout, “Nanoribbons of 2D materials: A review on emerging trends, recent developments and future perspectives,“ *Coord. Chem. Rev.* 453, (2022): 214335. <https://doi.org/10.1016/j.ccr.2021.214335>

30. Q. Chen, R. Song, C. Chen, X. Chen, “Tunable band gap of AlN/GaN nanoribbons and AlN/GaN nanoribbon heterojunctions: A first-principle study,” *Solid State Commun.* 172, (2013): 24. <http://dx.doi.org/10.1016/j.ssc.2013.08.026>

31. O. Brandt, L. Tapfer, K. Ploog, R. Bierwolf, M. Hohenstein, F. Phillip, H. Lage, A. Heberle, “InAs quantum dots in a single-crystal GaAs matrix,” *Phys. Rev.B* 44, no. 15 (1991): 8043. <https://doi.org/10.1103/PhysRevB.44.8043>

32. S. V. Ivanov, A. A. Toropov, T. V. Shubina, S. V. Sorokin, A. V. Lebedev, I. V. Sedova, and P. S. Kop’ev, G. R. Pozina, J. P. Bergman, and B. Monemar, “Growth and excitonic properties of single fractional monolayer CdSe/ZnSe structures,” *J. Appl. Phys.* 83, no. 6 (1998): 3168. <http://dx.doi.org/10.1063/1.367130>

33. N. N. Ledentsov, D. Bimberg, F. Hopfer, A. Mutig, V. A. Shchukin, A. V. Savel’ev, G. Fiol, E. Stock, H. Eisele, M. Dāhne, D. Gerthsen, U. Fischer, D. Litvinov, A. Rosenauer, S. S. Mikhrin, A. R. Kovsh, N. D. Zakharov, P. Werner, “Submonolayer Quantum Dots for High Speed Surface Emitting Lasers,” *Nanoscale Res. Lett.* 2, (2007):417. <http://dx.doi.org/10.1007/s11671-007-9078-0>

34. P. Lam, J. Wu, M. Tang, Q. Jiang, S. Hatch, R. Beanland, J. Wilson, R. Allison, H. Liu, “Submonolayer InGaAs/GaAs quantum dot solar cells,” *Sol. Energ. Mat. Sol. C.* 126, (2014): 83. <https://doi.org/10.1016/j.solmat.2014.03.046>

35. M. Asif Khan, J. N. Kuznia, D. T. Olson, T. George, and W. T. Pike, “GaN/AlN digital alloy short-period superlattices by switched atomic layer metalorganic chemical vapor deposition,” *Appl. Phys. Lett.* 63, (1993): 3470. <https://doi.org/10.1063/1.110123>

36. G. Kipshidze, V. Kuryatkov, B. Borisov M. Holtz, S. Nikishin, H. Temkin, “AlGaN-based ultraviolet light-emitting diodes grown on Si 111,” *Appl. Phys. Lett.* 80, No. 20, (2002): 3682. <https://doi.org/10.1063/1.1480886>

37. S. A. Nikishin, “III-Nitride Short Period Superlattices for Deep UV Light Emitters,” *Appl. Sci.*, 8, (2018): 2362. <https://doi.org/10.3390/app8122362>

38. V.N. Jmerik, T.V. Shubina, A.M. Mizerov, K.G. Belyaev, A.V. Sakharov, M.V. Zamoryanskaya, A.A. Sitnikova, V.Yu. Davydov, P.S. Kop’ev, E.V. Lutsenko b, N.V. Rzheutskii, A.V. Danilchik, G.P. Yablonskii, S.V. Ivanov, “AlGaN quantum well structures for deep-UV LEDs grown by plasma-assisted MBE using sub-monolayer digital-alloying technique,” *J. Cryst. Growth* 311, (2009): 2080. <https://doi.org/10.1016/j.jcrysgro.2008.11.080>

39. V.N. Jmerik, A.M. Mizerov, A.A. Sitnikova, P.S. Kop’ev, S.V. Ivanov, E.V. Lutsenko, N.P. Tarasuk, N.V. Rzheutskii, and G.P. Yablonskii, “Low-threshold 303 nm lasing in AlGaN-based multiple-quantum well structures with an asymmetric waveguide grown by plasma-assisted molecular beam epitaxy on c-sapphire,” *Appl. Phys. Lett.* 96, (2010): 141112.

40. K. Kamiya, Y. Ebihara, K. Shiraishi, M. Kasu, “Structural design of AlN/GaN superlattices for deep-ultraviolet lightemitting diodes with high emission efficiency,” *Appl. Phys. Lett.* 99, (2011): 151108. <http://dx.doi.org/10.1063/1.3651335>

41. P. Strak, P. Kempisty, M. Ptasinska, S. Krukowski, “Principal physical properties of GaN/AlN multiquantum well systems determined by density functional theory calculations,” *J. Appl. Phys.* 113, (2013): 193706. <http://dx.doi.org/10.1063/1.4805057>

42. Y. Taniyasu, M. Kasu, “Polarization property of deep-ultraviolet light emission from C-plane AlN/GaN shortperiod superlattices,” *Appl. Phys. Lett.* 99, (2011): 251112. <http://dx.doi.org/10.1063/1.3671668>

43. X. Rong, X. Wang, S. V. Ivanov, X. Jiang, G. Chen, P. Wang, W. Wang, C. He, T. Wang, T. Schulz, M. Albrecht, V. N. Jmerik, A. A. Toropov, V. V. Ratnikov, V. I. Kozlovsky, V. P. Martovitsky, P. Jin, F. Xu, X. Yang, Z. Qin, W. Ge, J. Shi, B. Shen, "High-Output-Power Ultraviolet Light Source from Quasi-2D GaN Quantum Structure," *Adv. Mater.* 28, (2016): 7978. <http://dx.doi.org/10.1002/adma.201600990>

44. D. Bayerl, SM Islam, C. M. Jones, V. Protasenko, D. Jena, E. Kioupakis, "Deep ultraviolet emission from ultra-thin GaN/AlN heterostructures," *Appl. Phys. Lett.* 109, (2016): 241102. <http://dx.doi.org/10.1063/1.4971968>

45. S. M. Islam, V. Protasenko, K. Lee, S. Rouvimov, J. Verma, H. (Grace) Xing, D. Jena, "Deep-UV emission at 219 nm from ultrathin MBE GaN/AlN quantum heterostructures," *Appl. Phys. Lett.* 111, (2017): 091104. <http://dx.doi.org/10.1063/1.5000844>

46. V. N. Jmerik, D. V. Nechaev, A. A. Toropov, E. A. Evropeitsev, V. I. Kozlovsky, V. P. Martovitsky, S. Rouvimov, S. V. Ivanov, "High-efficiency electron-beam-pumped sub-240-nm ultraviolet emitters based on ultra-thin GaN/AlN multiple quantum wells grown by plasma-assisted molecular-beam epitaxy on *c*-Al₂O₃," *Appl. Phys. Express* 11, (2018): 091003. <https://doi.org/10.7567/APEX.11.091003>

47. A. Harikumar, F. Donatini, C. Bougerol, E. Bellet-Amalric, Q. M. Thai, C. Dujardin, I. Dimkou, S. T. Purcell, E. Monroy, "Internal quantum efficiency of AlGaN/AlN quantum dot superlattices for electron-pumped ultraviolet sources," *Nanotechnology* 31, no.50, (2020): 505205. <http://dx.doi.org/10.1088/1361-6528/aba86c>

48. Y. Wu, X. Liu, P. Wang, D. A. Laleyan, K. Sun, Y. Sun, C. Ahn, M. Kira, E. Kioupakis, Z. Mi, "Monolayer GaN excitonic deep ultraviolet light emitting diodes," *Appl. Phys. Lett.* 116, (2020): 013101. <https://doi.org/10.1063/1.5124828>

49. V. Jmerik, D. Nechaev, K. Orekhova, N. Prasolov, V. Kozlovsky, D. Sviridov, M. Zverev, N. Gamov, L. Grieger, Y. Wang, T. Wang, X. Wang, S. Ivanov, "Monolayer-Scale GaN/AlN Multiple Quantum Wells for High Power e-Beam Pumped UV-Emitters in the 240–270 nm Spectral Range," *Nanomaterials* 11, (2021): 2553. <https://doi.org/10.3390/nano11102553>

50. V. Jmerik, D. Nechaev, A. Semenov, E. Evropeitsev, T. Shubina, A. Toropov, M. Yagovkina, P. Alexeev, B. Borodin, K. Orekhova, V. Kozlovsky, M. Zverev, N. Gamov, T. Wang, X. Wang, M. Pristovsek, H. Amano, S. Ivanov, "2D-GaN/AlN Multiple Quantum Disks/Quantum Well Heterostructures for High-Power Electron-Beam Pumped UVC Emitters," *Nanomaterials* 13, (2023): 1077. <https://doi.org/10.3390/nano13061077>

51. A. A. Toropov, E. A. Evropeitsev, M. O. Nestoklon, D. S. Smirnov, T. V. Shubina, V. Kh. Kaibyshev, G. V. Budkin, V. N. Jmerik, D. V. Nechaev, S. Rouvimov, S. V. Ivanov, B. Gil, "Strongly Confined Excitons in GaN/AlN Nanostructures with Atomically Thin GaN Layers for Efficient Light Emission in Deep-Ultraviolet," *Nano Lett.* 20, (2020): 158. <https://doi.org/10.1021/acs.nanolett.9b03517>

52. R. Vermeersch, G. Jacopin, F. Castioni, J.-L. Rouvière, A. García-Cristóbal, A. Cros, J. Pernot, B. Daudin, "Ultrathin GaN quantum wells in AlN nanowires for UV-C emission," *Nanotechnology* 34, (2023): 275603. <https://doi.org/10.1088/1361-6528/accaeb>

53. J. Nicholls, L. Anderson, W. Lee, J. J. Seok Ahn, A. Baskaran, H. Bang, M. Belloeil, Y. Cai, J. Campbell; J. Chai, N. Corpuz; V. Entoma, B. Hayden, T. Hung; H. Kim, D. King, S. Li, A. Liu, D. McMahon, V. Nguyen, S. Fong Pan, S. Tedman-Jones, W. J. Toe, R. Tsai, M. P. Tudo, H. P. Wang, Y. Wang, S. Yan, R. Yang, K. Yeo, W. Schaff, N. Krause, R. Charters, J. Tang, P. Atanackovic, "High performance and high yield sub-240 nm AlN:GaN short period superlattice LEDs grown by

MBE on 6 in. sapphire substrates featured, " *Appl. Phys. Lett.* 123, (2023): 051105. <https://doi.org/10.1063/5.0160177>

54. N. Mokutani, M. Deura, S. Mouri, K. Shojiki, S. Xiao, H. Miyake, T. Araki, "Control of Metal-Rich Growth for GaN/AlN Superlattice Fabrication on Face-to-Face-Annealed Sputter-Deposited AlN Templates," *Phys. Status Solidi B* 260, no.9 (2023): 2300061. <https://doi.org/10.1002/pssb.202300061>

55. S. Li, X. Liang, P. Shao, S. Chen, Z. Li, X. Su, T. Tao, Z. Xie, M. A. Khan, L. Wang, T. T. Lin, H. Hirayama, B. Liu, D. Chen, K. Wang, R. Zhang, "Monolayer-scale AlN/GaN digital alloys grown by plasma-assisted molecular beam epitaxy," *Appl. Phys. Lett.* 125, (2024): 112102. <https://doi.org/10.1063/5.0215886>

56. W. Lee, Y. Wu, M. Florian, Z. Mi, M. Kira, E. Kioupakis, "Charge-Transfer Excitons in Coupled Atomically Thin Polar Nitride Quantum Wells," *Nano Lett.* 25, (2025): 3045. <https://doi.org/10.1021/acs.nanolett.4c04593>

57. N. Gao, X. Feng, S. Lu, W. Lin, Q. Zhuang, H. Chen, K. Huang, S. Li, J. Kang, "Integral Monolayer-Scale Featured Digital-Alloyed AlN/GaN Superlattices Using Hierarchical Growth Units," *Cryst. Growth Des.* 19, (2019):1720. <http://dx.doi.org/10.1021/acs.cgd.8b01677>

58. Y. Wang, X. Rong, S. Ivanov, V. Jmerik, Z. Chen, H. Wang, T. Wang, P. Wang, P. Jin, Y. Chen, V. Kozlovsky, D. Sviridov, M. Zverev, E. Zhdanova, N. Gamov, V. Studenov, H. Miyake, H. Li, S. Guo, X. Yang, F. Xu, T. Yu, Z. Qin, W. Ge, B. Shen, X. Wang, "Deep Ultraviolet Light Source from Ultrathin GaN/AlN MQW Structures with Output Power Over 2 Watt," *Adv. Optical Mater.* 7, no.10 (2019): 1801763. <http://dx.doi.org/10.1002/adom.201801763>

59. H. Kobayashi, S. Ichikawa, M. Funato, Y. Kawakami, "Self-Limiting Growth of Ultrathin GaN/AlN Quantum Wells for Highly Efficient Deep Ultraviolet Emitters," *Adv. Optical Mater.* 7, no.21 (2019): 1900860. <http://dx.doi.org/10.1002/adom.201900860>

60. Y. Wang, Y. Yuan, R. Tao, S. Liu, T. Wang, S. Sheng, P. Quach, M. Kumar CM, Z. Chen, F. Liu, Xin Rong, Peng Jin, M. Feng, H. Li, S. Guo, W. Ge, J. K. Lee, B. Shen, X. Wang, "High-Efficiency E-Beam Pumped Deep-Ultraviolet Surface Emitter Based on AlGaN Ultra-Thin Staggered Quantum Wells," *Adv. Optical Mater.* 10, no.18 (2022): 2200011. <http://dx.doi.org/10.1002/adom.202200011>

61. M. Funato, H. Kobayashi, Y. Kawakami, "Confinement of Excitons within GaN 1D Nanoarchitectures Formed on AlN Molecular Steps," *Adv. Optical Mater.* 12, no.12 (2024): 2302506. <http://dx.doi.org/10.1002/adom.202302506>

62. V. Jmerik, A. Toropov, V. Davydov, S. Ivanov, "Monolayer-Thick GaN/AlN Multilayer Heterostructures for Deep-Ultraviolet Optoelectronics," *Phys. Status Solidi RRL* 15, (2021): 2100242. (Review) <https://doi.org/10.1002/pssr.202100242>

63. M. Funato, Y. Kawakami, "Singularity structures for sub-250nm emissions from AlGaN-based semiconductors, STAP REVIEW" *Jap. J. Appl. Phys.* 60, (2021): 120501. <https://doi.org/10.35848/1347-4065/ac2f1e>

64. H. Mariette, "Formation of self-assembled quantum dots induced by the Stranski-Krastanow transition: a comparison of various semiconductor systems," *C. R. Physique* 6, (2005): 23. <http://dx.doi.org/10.1016/j.crhy.2004.11.003>

65. A. Ichimiya, P. I . Cohen, Reflection high-energy electron diffraction, (Cambridge, UK: Cambridge University Press, 2004), ISBN 0521453739.

66. P. Kruse, M. Schowalter, D. Lamoen, A. Rosenauer, D. Gerthsen, "Determination of the mean inner potential in III-V semiconductors, Si and Ge by density functional theory and electron holography," *Ultramicroscopy* 106, (2006):105. <http://dx.doi.org/10.1016/j.ultramic.2005.06.057>

67. J. E. Northrup, J. Neugebauer, R. M. Feenstra, A. R. Smith, "Structure of GaN (0001): The laterally contracted Ga bilayer model," *Phys. Rev. B* 61, no.15 (2000): 9932. <http://dx.doi.org/10.1103/physrevb.61.9932>

68. G. Koblmüller, R. Averbeck, H. Riechert, P. Pongratz, "Direct observation of different equilibrium Ga adlayer coverages and their desorption kinetics on GaN (0001) and (0001⁻). Surfaces," *Phys. Rev. B* 69, (2004): 035325. <https://doi.org/10.1103/PhysRevB.69.035325>

69. C. V. Thompson, "Solid-State Dewetting of Thin Films," *Annu. Rev. Mater. Res.* 42, (2012): 399. <http://dx.doi.org/10.1146/annurev-matsci-070511-155048>

70. J. H. Neave, P. J. Dobson, B. A. Joyce, and Jing Zhang, "Reflection high energy electron diffraction oscillations from vicinal surfaces—a new approach to surface diffusion measurements," *Appl. Phys. Lett.* 47, (1985): 100. <http://dx.doi.org/10.1063/1.96281>

71. A-L. Barabási, H.E. Stanley, Submonolayer deposition. In: *Fractal Concepts in Surface Growth*. Cambridge University Press; 1995:175-191. <https://doi.org/10.1017/CBO9780511599798.019>

72. W. K. Burton, N. Cabrera and F. C. Frank, "The Growth of Crystals and the Equilibrium Structure of Surfaces," *Philos. Trans. R. Soc. London, Ser. A* 243, (1951): 299. <https://doi.org/10.1098/rsta.1951.0006>

73. M. A. Laurent, S. Keller, U. K. Mishra, "Comprehensive Analysis of Surface Morphology and Growth Mode of AlInGaN Films," *Phys. Status Solidi A*, 216, (2019): 1800523. <https://doi.org/10.1002/pssa.201800523>

74. W.A. Harrison: Electronic Structure and the Properties of Solids: The Physics of the Chemical Bond, (Dover, New York 1989)

75. N. A.K.Kaufmann, L.Lahourcade, B.Hourahine, D.Martin, N.Grandjean, "Critical impact of Ehrlich–Schwöbel barrier on GaN surface morphology during homoepitaxial growth," *J.Cryst. Growth* 433, (2016): 36. <http://dx.doi.org/10.1016/j.jcrysgro.2015.06.013>

76. G.Ehrlich, F.G. Hudda, "Atomic view of surface self-diffusion: Tungsten on tungsten," *J. Chem. Phys.* 44, no.3. (1966): 1039. <https://doi.org/10.1063/1.1726787>

R. L. Schwoebel, E. J. Shipsey, "Step Motion on Crystal Surfaces," *J. Appl. Phys.* 37, (1966): 3682. <http://dx.doi.org/10.1063/1.1707904>

77. P.F. Fewster, "X-ray diffraction from low-dimensional structures," *Semicond. Sci. Technol.* 8, (1993): 1915. <https://doi.org/10.1088/0268-1242/8/11/001>

78. B. Jenichen, S.A. Stepanov, B. Brar, H. Kroemer, "Interface roughness of InAs/AlSb superlattices investigated by x-ray scattering," *J.Appl.Phys.* 79, (1996): 120. <https://doi.org/10.1063/1.360918>

79. M. Shishkin, G. Kresse, "Self-consistent GW calculations for semiconductors and insulators," *Phys. Rev. B* 75, (2007): 235102. <https://doi.org/10.1103/PhysRevB.75.235102>

80. J.P. Perdew, "Density functional theory and the band gap probleproblem", *Int. J. Quantum Chem.* 28, (1986): 497. <https://doi.org/10.1002/qua.560280846>

81. V. Davydov, E. Roginskii, Y. Kitaev, A. Smirnov, I. Eliseyev, D. Nechaev, V. Jmerik, M. Smirnov, "Phonons in Short-Period GaN/AlN Superlattices: Group-Theoretical Analysis, Ab initio Calculations, and Raman Spectra," *Nanomaterials* 11, (2021): 286. <https://doi.org/10.3390/nano11020286>

82. A.J. Morris, R.J.Nicholls, C.J. Pickard, J.R.Yates, "OptaDOS: A tool for obtaining density of states, core-level and optical spectra from electronic structure codes," *Comput. Phys. Commun.* 185, no.5, (2014): 1477. <http://dx.doi.org/10.1016/j.cpc.2014.02.013>

83. V. Jmerik, V. Kozlovsky, X. Wang, "Electron-Beam-Pumped UVC Emitters Based on an (Al,Ga)N Material System," (Review) *Nanomaterials*, 13, (2023): 2080. <https://doi.org/10.3390/nano13142080>

84. V. I. Kozlovsky, M. M. Zverev, A.N. Semenov, D.V. Nechaev, D.E. Sviridov, Ya.K., Skasyskii, V.N. Jmerik, "Nonequilibrium carriers in GaN/AlN heterostrcutures: Diffusion in barrier layers and trapping in monolayer quantum wells," *JETP* 140, no. 6 (2025):. <https://doi.org/10.31857/S0044451025060070>

85. M. H. Xie, S. M. Seutter, W. K. Zhu, L. X. Zheng, Huasheng Wu, S. Y. Tong, "Anisotropic Step-Flow Growth and Island Growth of GaN(0001) by Molecular Beam Epitaxy," *Phys. Rev. Lett.* 82, no.13 (1999): 2252. <https://doi.org/10.1103/PhysRevLett.85.2352>

86. V.N. Jmerik, D.V. Nechaev, S.V. Ivanov, "Kinetics of metal-rich PA molecular beam epitaxy of AlGaN heterostructures for mid-UV photonics," in Molecular Beam Epitaxy: from Research to Mass Production, 2nd ed.; Henini, M., Ed.; (Amsterdam, Netherlands, Oxford, UK, Cambridge, USA: Elsevier Inc., 2018). pp. 135–179. ISBN: 9780128121368 <https://doi.org/10.1016/B978-0-12-812136-8.00008-6>

87. D.V. Nechaev, O.A. Koshelev, V.V. Ratnikov, P.N. Brunkov, A.V. Myasoedov, A. A. Sitnikova, S.V. Ivanov, V.N. Jmerik, "Effect of stoichiometric conditions and growth mode on threading dislocations filtering in AlN/c-Al₂O₃ templates grown by PA MBE," *Superlattices and Microst.* 138, (2020): 106368. <https://doi.org/10.1016/j.spmi.2019.106368>

88. X. Gonze,, B. Amadon, P.-M. Anglade, J.-M. Beuken, F. Bottin, P. Boulanger, F. Bruneval, D. Caliste, R. Caracas, M. Côté, T. Deutsch, L. Genovese, Ph. Ghosez, M. Giantomassi, S. Goedecker, D.R. Hamann, P. Hermet, F. Jollet, G. Jomard, S. Leroux, M. Mancini, S. Mazeved, M.J.T. Oliveira, G. Onida, Y. Pouillon, T. Rangel, G.-M. Rignanese, D. Sangalli, R. Shaltaf, M. Torrent, M.J. Verstraete, G. Zerah, J.W. Zwanziger, "ABINIT: First-principles approach to material and nanosystem properties," *Comput. Phys. Commun.* 180, (2009): 2582. <https://doi.org/10.1016/j.cpc.2009.07.007>

89. X. Gonze, I. Gian-Marco Rignanese, M. Verstraete, J.-M. Beuken, Y. Pouillon, R. Caracas, F. Jollet, M. Torrent, G. Zerah, M. Mikami, P. Ghosez, M. Veithen, J.-Y. Raty, V. Olevano, F. Bruneval, L. Reining, R. Godby, G. Onida, D. R. Hamann, D. C. Allan, "A brief introduction to the ABINIT software package," *Z. Kristallogr.* 220, (2005): 558. <https://doi.org/10.1524/zkri.220.5.558.65066>

9.0 H. J. Monkhorst, J. D. Pack, "Special points for Brillouin-zone integrations," *Phys. Rev. B* 13, no.12 (1976): 5188. <https://doi.org/10.1103/physrevb.13.5188>

91. W. G. Aulbur, L. Jönsson, J. W. Wilkins, "Quasiparticle Calculations in Solids, Solid State Physics vol. 54, (Amsterdam, Netherlands: Elsevier BV, 2000), ISBN O-LZ-M)7754-I. [https://doi.org/10.1016/s0081-1947\(08\)60248-9](https://doi.org/10.1016/s0081-1947(08)60248-9)

92. S. Lebègue, B. Arnaud, M. Alouani, P. E. Bloechl, "Implementation of an All-Electron GW Approximation Based on the Projector Augmented Wave Method Without Plasmon Pole Approximation: Application to Si, SiC, AlAs, InAs, NaH, and KH," *Phys. Rev. B* 67, (2003): 155208. <https://doi.org/10.1103/physrevb.67.155208>

Supporting Information

Fractional-monolayer 2D-GaN/AlN structures: growth kinetics and UVC-emitter application

Valentin Jmerik*, Dmitrii Nechaev, Evgenii Evropeitsev, Evgenii Roginskii, Maria Yagovkina, Prokhor Alekseev, Alexey Semenov, , Vladimir Kozlovsky, Mikhail Zverev, Nikita Gamov, Tao Wang, Xinqiang Wang, Tatiana Shubina, Alexey Toropov

SI. Additional information

To investigate the GaN growth on the surface of AlN barrier layers in $250 \times \{\text{GaN}_{1.5}/\text{AlN}_{15}\}$ MQW structures, GaN test layers with different nominal thicknesses $t_{\text{GaN}} = 10$ and 20 ML were grown at $\phi_{\text{Ga}}/\phi_{\text{N}_2^*} = 1.1$ and 2.1 , respectively. A full analysis of the critical thicknesses in these layers for the 2D-3D transition in the growth mode will be presented elsewhere. For this article, it is important that this thickness, corresponding to the transition from descending to ascending evolution of the RHEED intensity, exceeds 2 MLs, as shown in Figure S1a,b.

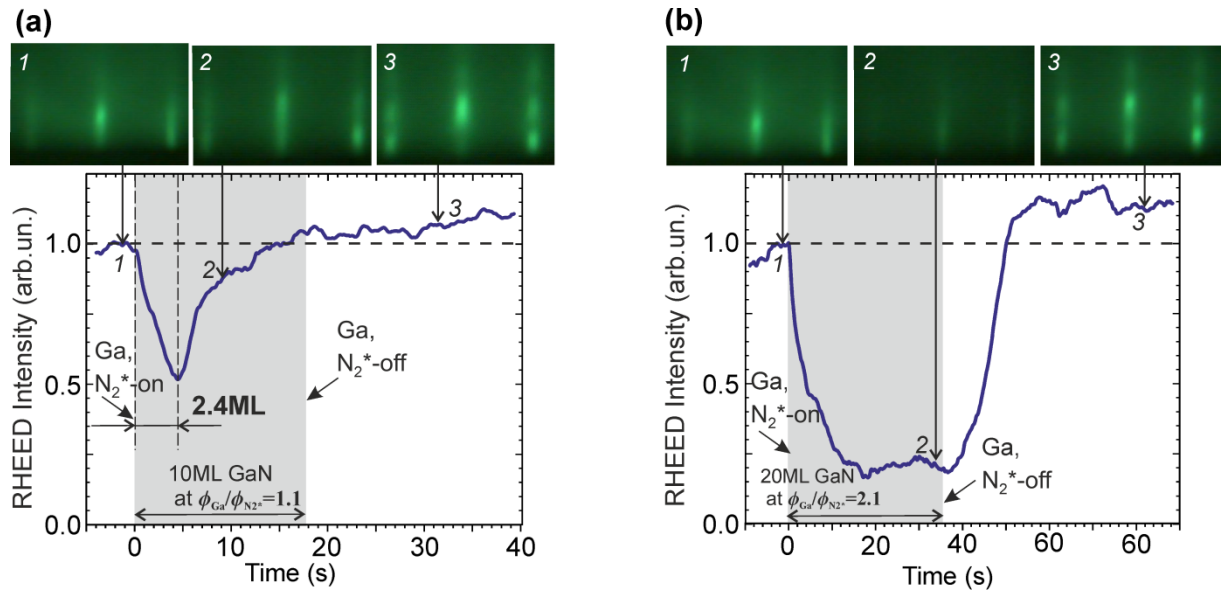


Figure S1. Time evolution of RHEED specular reflectance intensity during growth of GaN layers on an AlN with a thickness of 10ML at $\phi_{\text{Ga}}/\phi_{\text{N}_2^*} = 1.1$ (a) and with a thickness of 20ML at $\phi_{\text{Ga}}/\phi_{\text{N}_2^*} = 2.1$ (b).

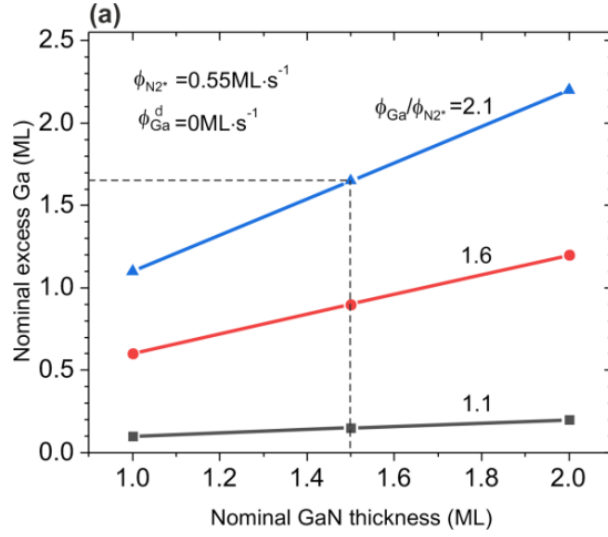


Figure S2. (a) Calculated dependences of nominal excess Ga adlayer thickness accumulated during the growth of GaN with a thickness from 1 to 2ML under different flux ratio $\phi_{\text{Ga}}/\phi_{\text{N}2^*}=1.1, 1.6, 2.1$ and the same $\phi_{\text{N}2^*}=0.55\text{ML}\cdot\text{s}^{-1}$, assuming negligible Ga-desorption ($\phi_{\text{Ga}}^{\text{d}}=0$).

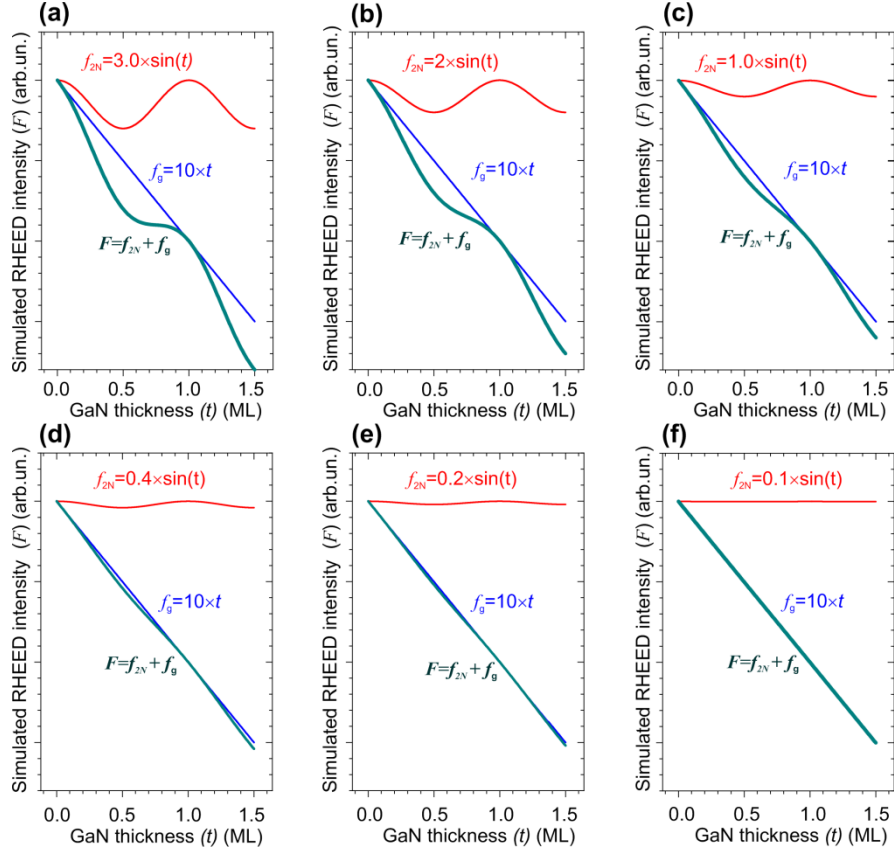


Figure S3. Simulation results of the temporal changes in the total RHEED intensity $F=f_{2N}+f_g$ (where f_{2N}, f_g are the oscillation and linear factors, respectively) during the initial growth of a 1.5-ML-thick GaN/AlN QW. Graphs (a) - (c) illustrate the change in F with decreasing in the f_{2N} at the same f_g .

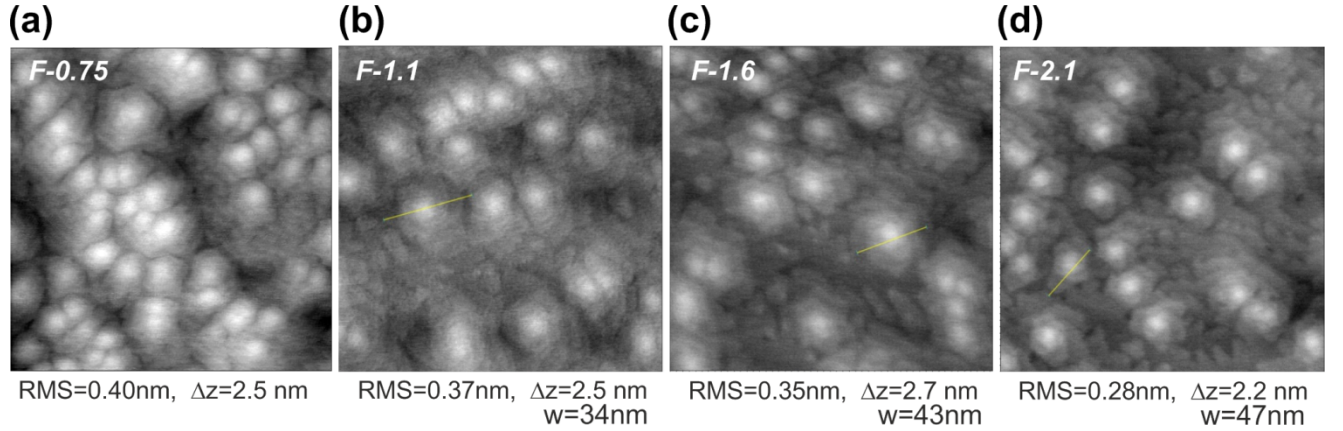


Figure S4. AFM images ($1 \times 1 \mu\text{m}^2$) of the AlN top surfaces of F -series $250 \times \{\text{GaN}_{1.5}/\text{AlN}_{16}\}$ MQWs structures grown at the different $\phi_{\text{Ga}}/\phi_{\text{N}_2^*}$: 0.8 (a), 1.1 (b), 1.6 (c), 2.1(d).

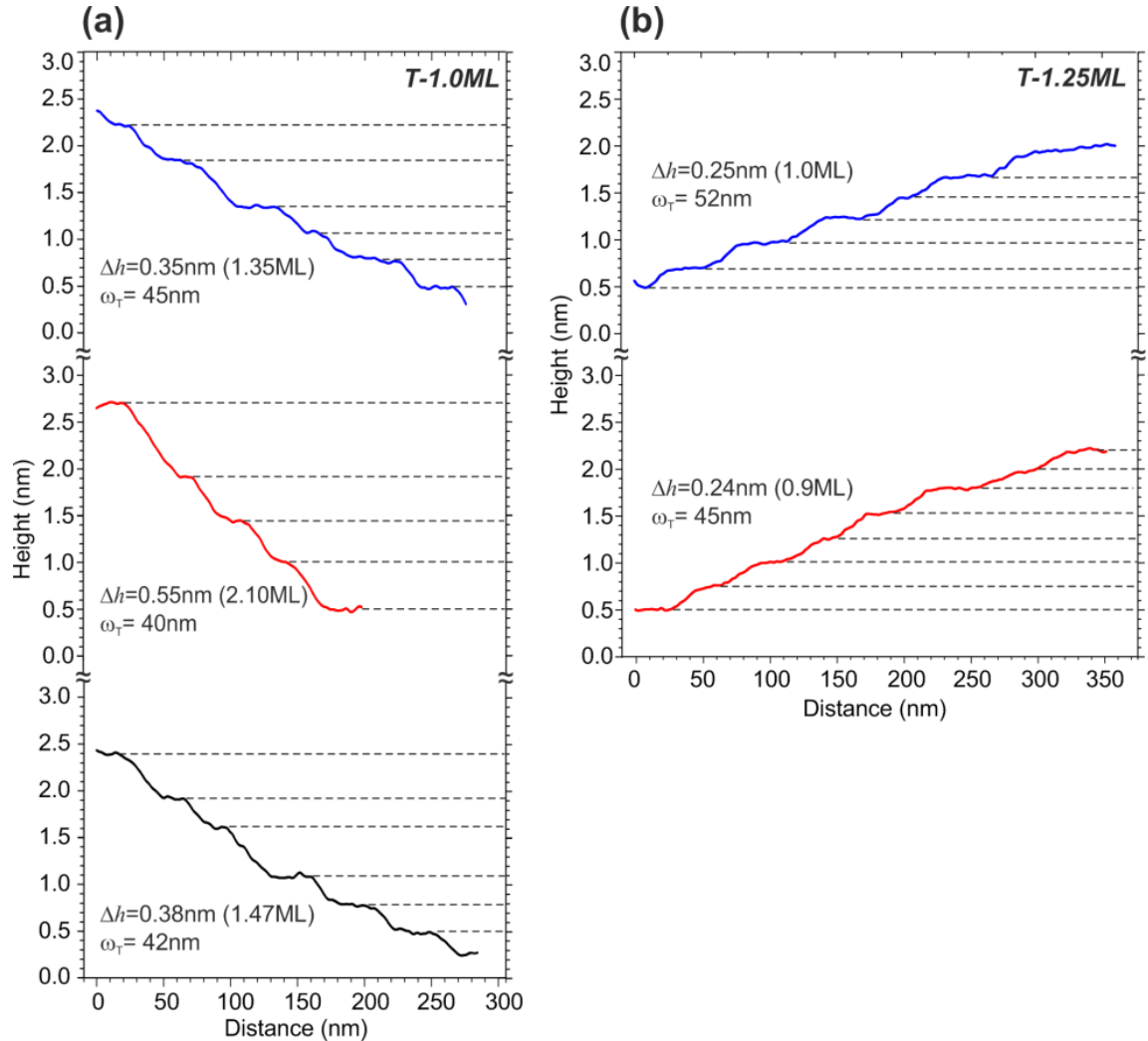


Figure S5. Height profiles measured at different positions in AFM images of the MQW structures T -1.0ML (a) and T -1.25ML (b). The average step heights (Δh) and terrace widths (ω_T) are shown in each graph.

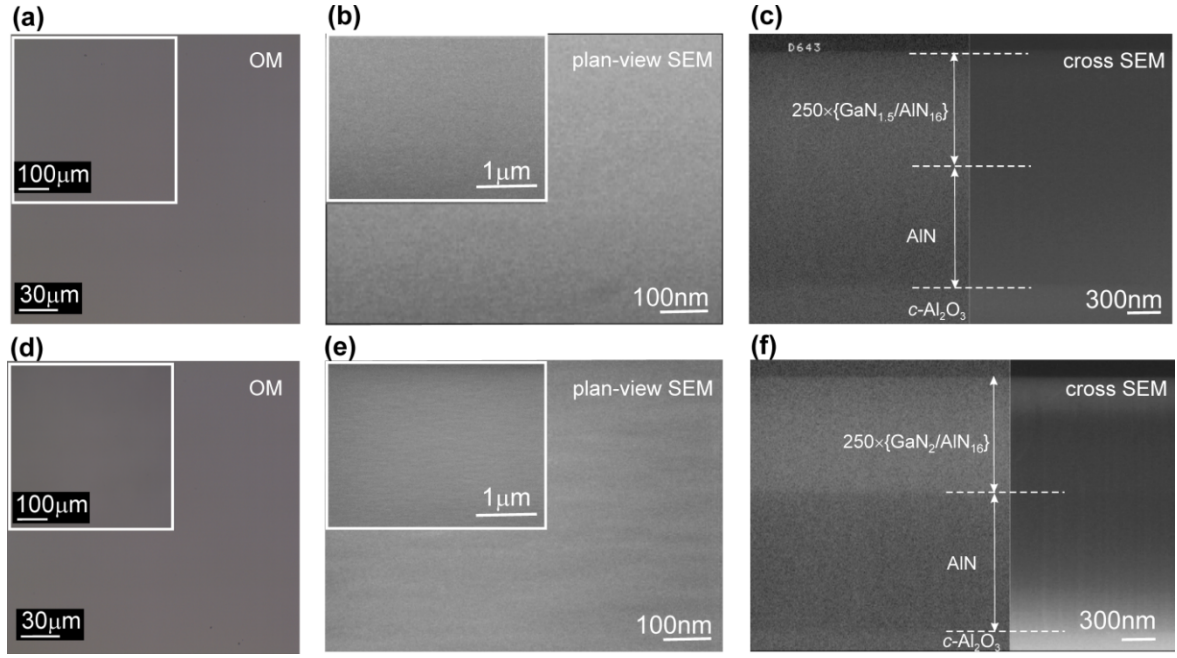


Figure S6. Optical microscope (a,d) and scanning electron microscope (SEM) images (b,c,e,f) of two structures T -1.5ML (a-c) and T -2.0ML (d-f). The cross-view SEM image (f) of $250\{\text{GaN}_m/\text{AlN}_{16}\}$ MQWs on AlN/c-Al₂O₃ layer shows a contrast in Ga content between these regions, whereas the analogous SEM image (c) of $250\{\text{GaN}_{1.5}/\text{AlN}_{16}\}$ on the same AlN/c-Al₂O₃ does not show such a contrast.

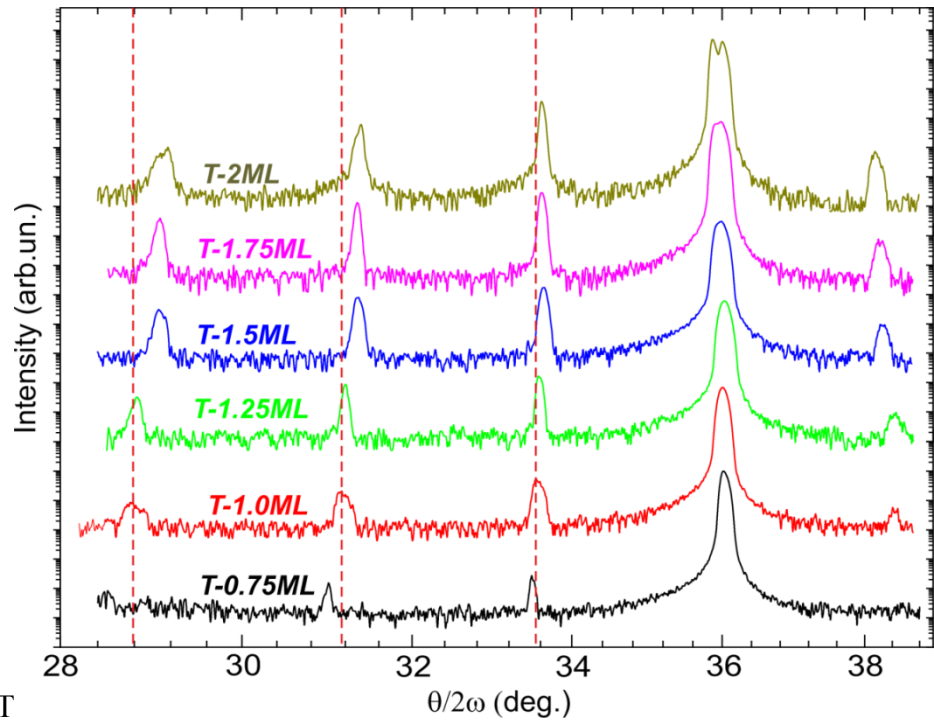


Figure S7. $\theta/2\omega$ -scans of the X-ray diffraction curves of the symmetric reflection (0002) for the T-series $250\{\text{GaN}_m/\text{AlN}_{16}\}$ MQW structures ($m = 0.75\text{--}2\text{ML}$).

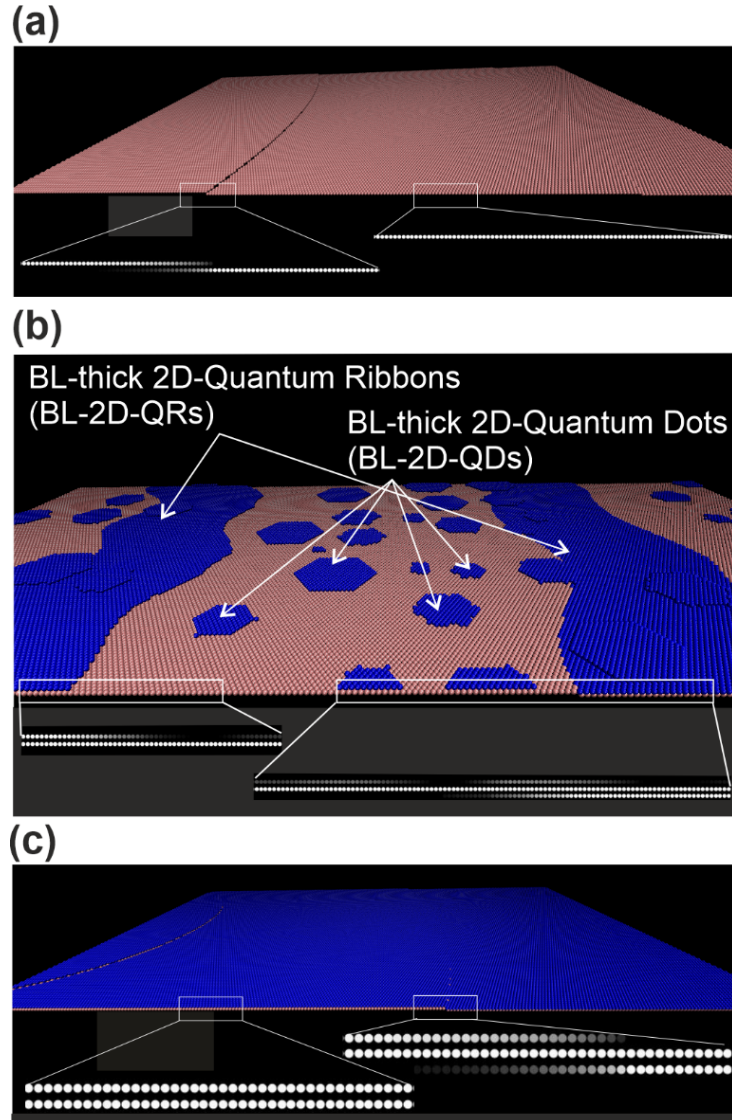


Figure S8. Schematic representations of the GaN_m/AlN QWs with various nominal thickness (m) and GaN relative content between QR (n_{QR}) and QD- (n_{QD}) phases in the upper layer: (a) $m=1\text{ML}$, (b) $m=1.5\text{ML}$, $n_{\text{QR}}=30$ $n_{\text{QD}}=20\%$; $m=2\text{ML}$ (c) . These images were simulated using VMD 2.0 software, taking into account both the 2D-nucleation and step-flow growth mechanisms of GaN quantum wells. The bottom insets in each figure displays the corresponding thickness-averaged projections from the regions indicated by white rectangles, which simulate cross-sectinal HAADF-STEM images of GaN QWs.

The accuracy of the G_0W_0 method was verified by comparing the calculated electronic structures of symmetric short-period $\text{GaN}_m/\text{AlN}_n$ $m=n=3,4,6,8$ superlattices, as well as asymmetric heterostructures with a constant QW thickness $m=1.5$ and variable values $n=2-16$, grown, as described in Ref.81. Figure S9 shows satisfactory agreement (with a systematic error of ~ 0.2 eV) between the effective band gap (E_g^*) values calculated using the DFT method and the experimental values of this characteristic determined from the optical absorption spectra. Note that both the calculated and experimental values of E_g^* begin to change only at barrier layer thicknesses less than 8 ML, which corresponds to the data of Sun *et al.*^[S1], who calculated the critical thickness of the onset of overlap of wave functions of carriers in adjacent QWs to be equal to $\sim 7-9$ ML. Therefore, all calculations in this work were carried out for $m=10-12$, but their results should also be valid for MQW structures with larger AlN thicknesses, including $n=15$.

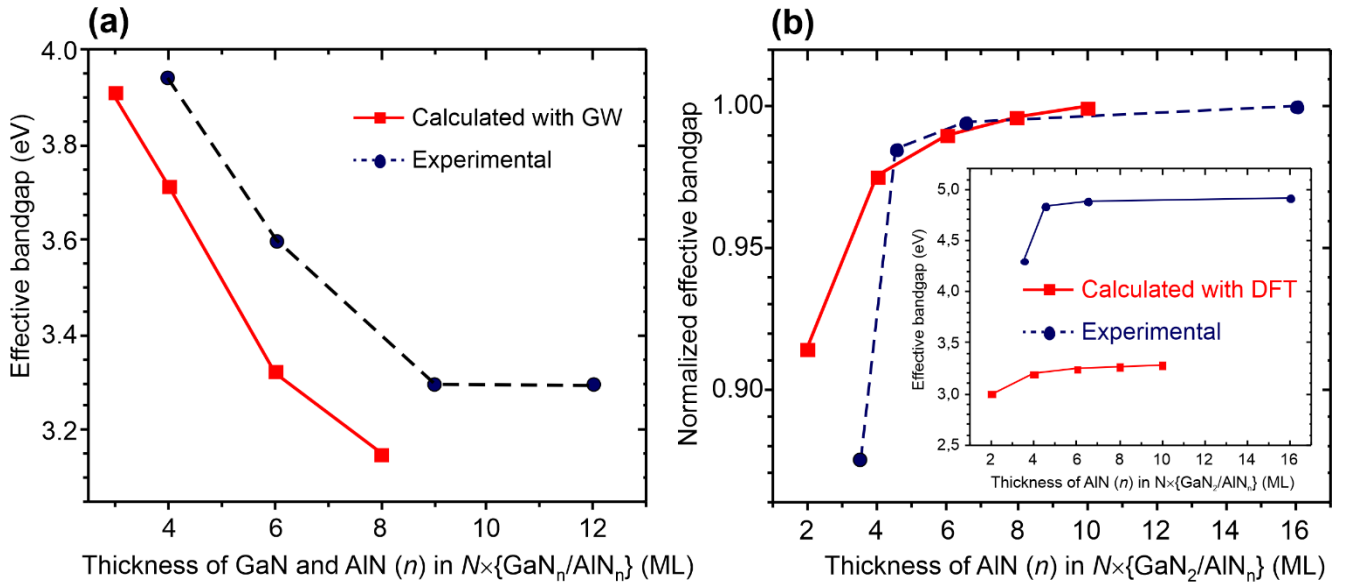


Figure S9. (a) The calculated by G_0W_0 method (red, solid) and experimental (blue, dashed) dependences of effective band gaps E_g^* on AlN thickness (n) in $N \times \{\text{GaN}_n/\text{AlN}_n\}$ superlattices. (b) The calculated by DFT method (red, solid) and experimental (blue, dashed) dependences of effective band gaps E_g^* on AlN thickness (n) in $N \times \{\text{GaN}_2/\text{AlN}_n\}$ heterostructures. In both experimental studies, the band gaps were determined from optical adsorption spectra.

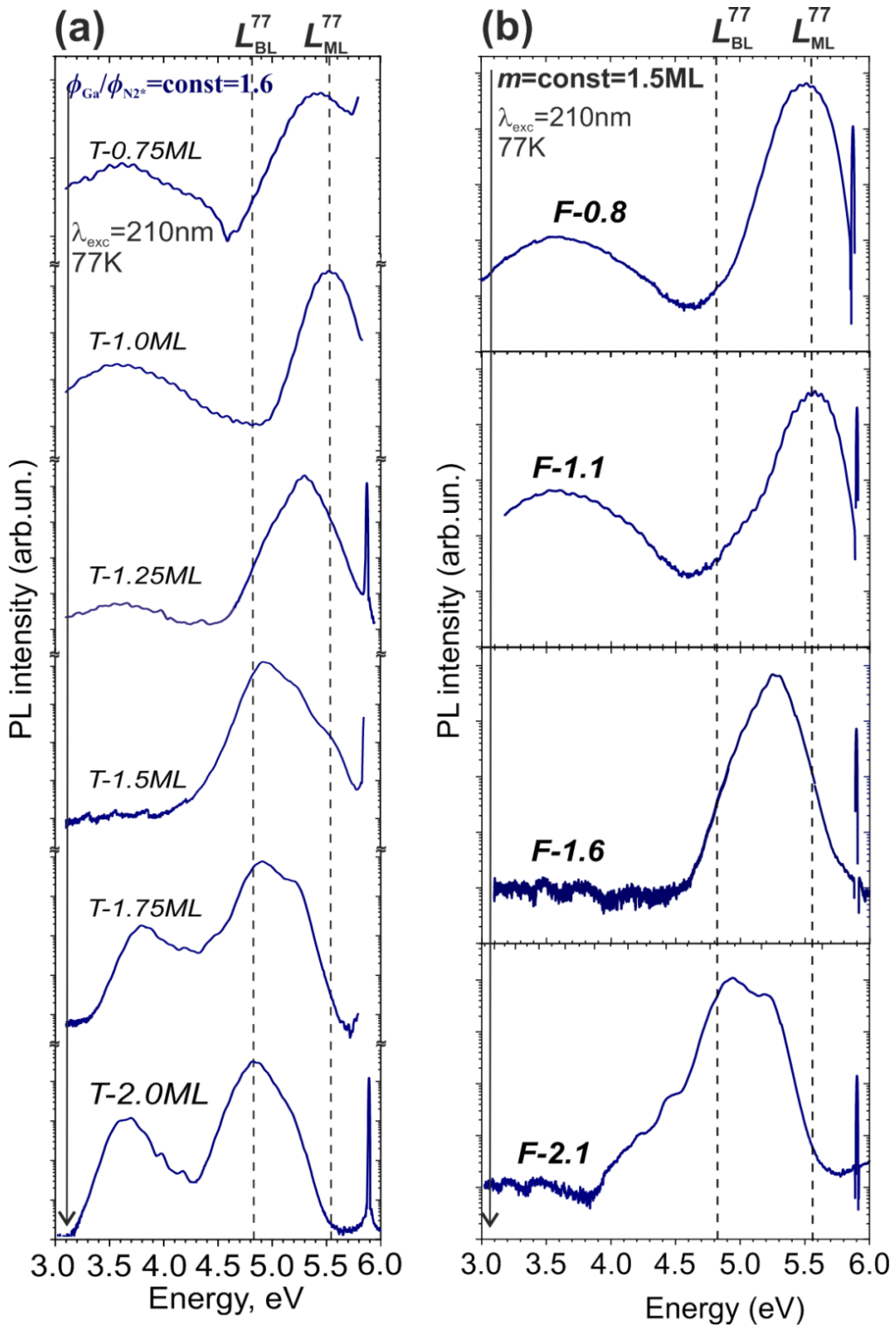


Figure S10. PL spectra (77K) of samples from the T-series (a) and F-series (b)., presented on a semi-logarithmic scale.

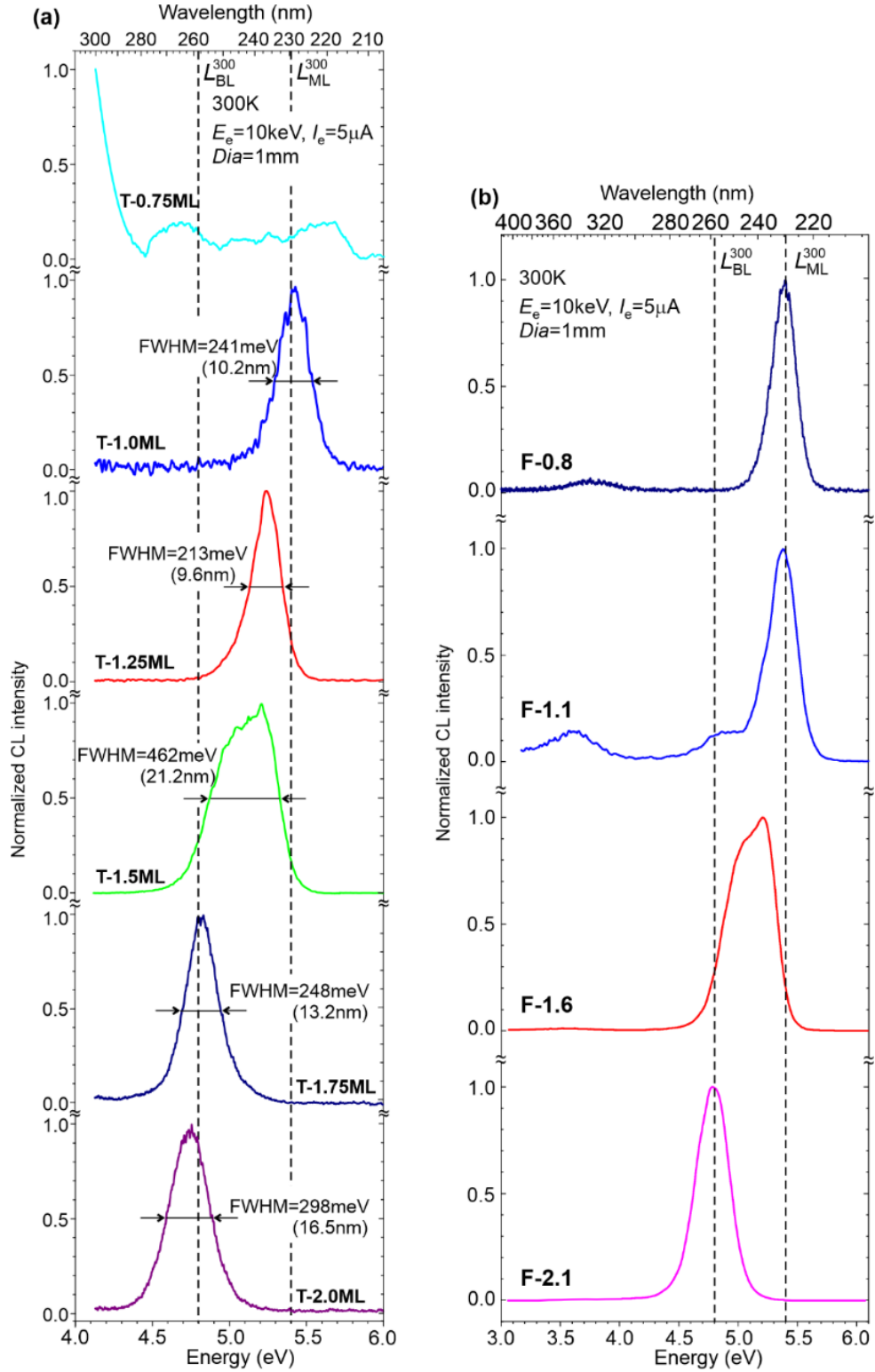


Figure S11. CL spectra (300K) of the T -series $250 \times \{\text{GaN}_m/\text{AlN}_{16}\}$ ($m=0.75\text{-}2\text{ML}$) MQW structures (a) and F -series $250 \times \{\text{GaN}_{1.5}/\text{AlN}_{16}\}$ ($\phi_{\text{Ga}}/\phi_{\text{N}2^*} = 0.8, 1.1, 1.6, 2.1$) (b), excited using a low-current e-gun with $I_e=5\mu\text{A}$ and $U_e=10\text{keV}$.

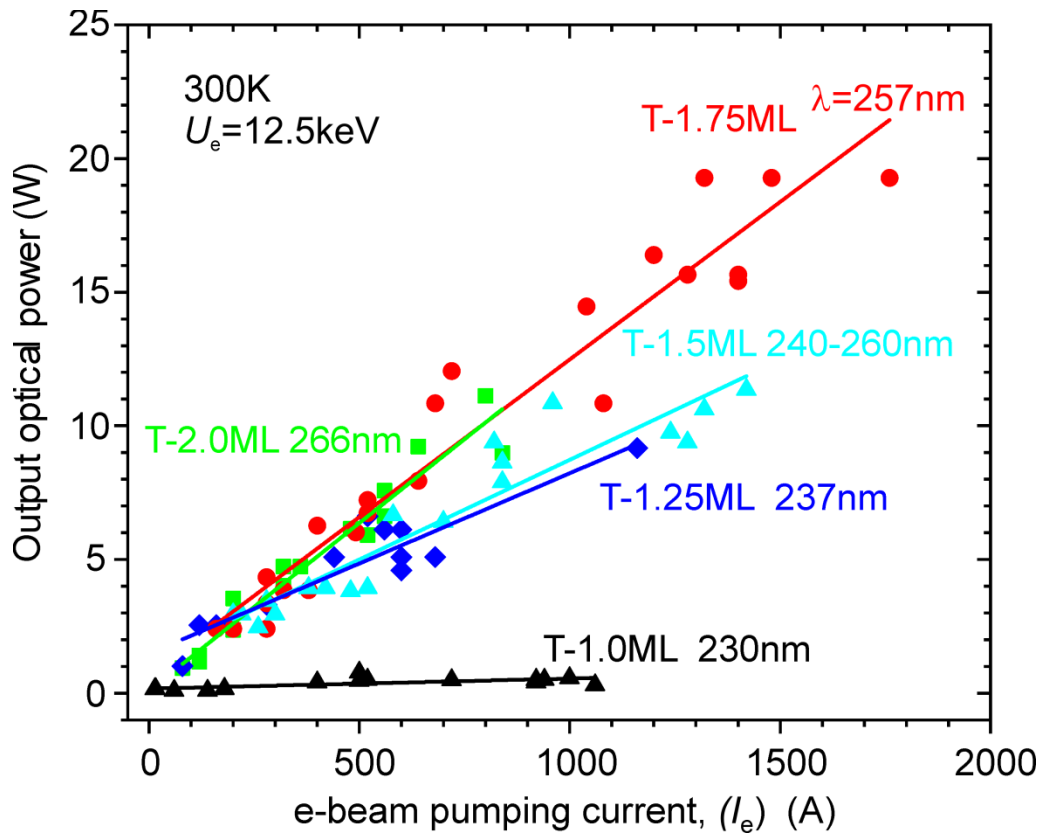


Figure S12. Current dependences of the peak optical output powers ($P(I_e)$) of the T -series structures: T -1.0, T -1.25, T -1.5, T -1.75, T -2.0, those low-current CL spectra are shown in Figure S11a.

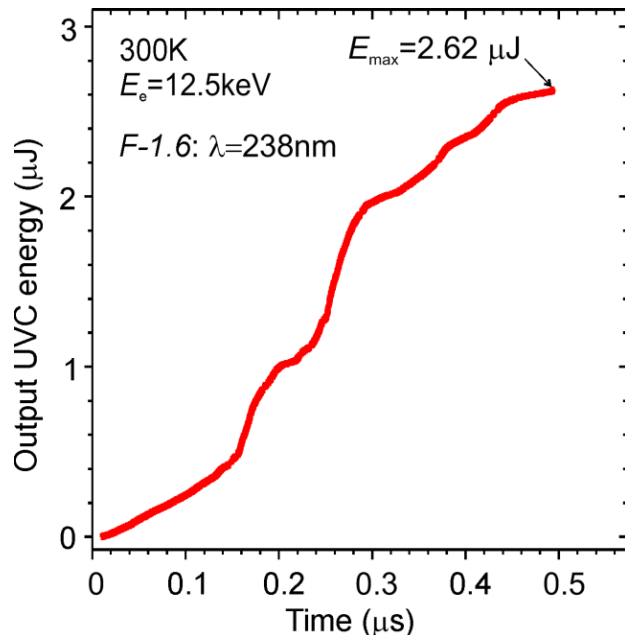


Figure S13. Time variation of the output optical energy of UVC radiation during one high current e-beam pumping pulse of the F -1.6 structure.

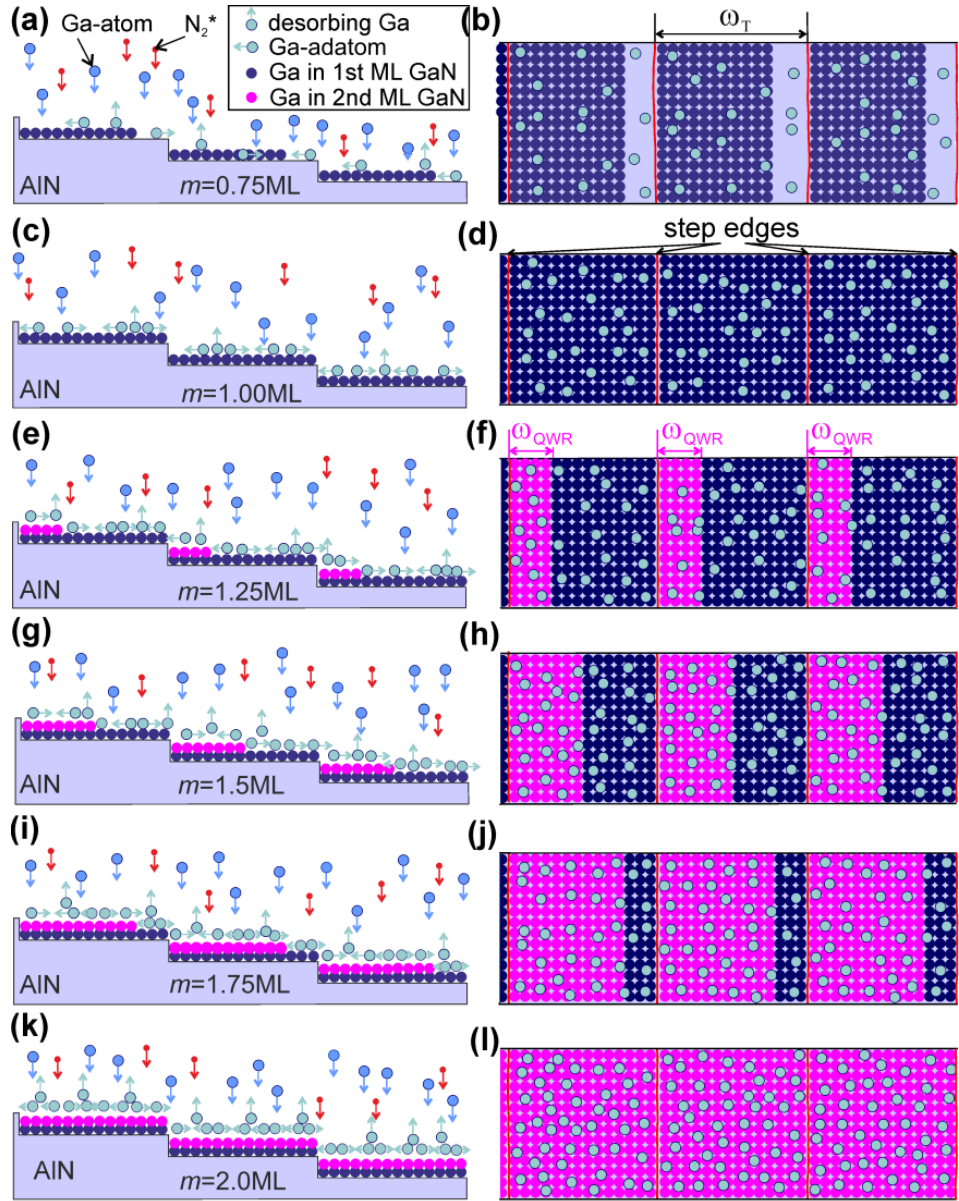


Figure S14. Scheme of the “ideal” layer by layer growth of GaN/AlN QW with $m = 0.75\text{-}2\text{ML}$ under Ga-enriched growth conditions in accordance with the step-flow growth mechanism only (without taking into account 2D-nucleation growth mechanism).

SII. Electron-beam pumping of GaN/AlN heterostructures: design and technique for measuring the electron beam current, output optical power and optical spectra

A. General scheme

Figure S15 shows a schematic of the setup used for e-beam pumping of GaN/AlN MQW heterostructures and detection of both the e-beam current and the output UVC radiation.

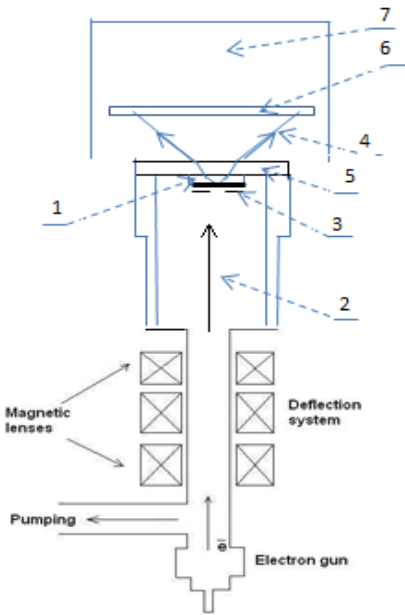


Figure S15. Scheme of the experimental setup, consisting of: 1 – sample with excited structure, 2 - electron beam, 3 - diaphragm in front of the sample, 4 - sample radiation, 5 - sapphire window of the camera, 6 - radiation detector photocathode, 7 - FEK-22 photodetector.

B. Electron-beam gun with a plasma cathode

The setup above used an e-gun with a so-called plasma cathode, in which the plasma formed as a result of breakdown over the surface of a ferroelectric^[S2]. The characteristics of such *e*-guns are detailed in Refs. S3–S6 and have been recently reviewed in Ref. 83. Figure S16 shows the specific design of a e-gun used in this work. The cathode of the electron gun was a ferroelectric plate 2–3 mm thick with metallized surfaces coated on the outside with a dielectric material. In one place, the plate is notched, and when a high voltage pulse from a pulse transformer was applied between the metallized surfaces, a breakdown occurred along the surface of the ferroelectric at the notch. The anode of the gun was a stainless-steel tube with polished surfaces, located at ground potential. The triggering frequency was determined by the repetition rate of the triggering pulses and was 1.5 or 12 Hz.

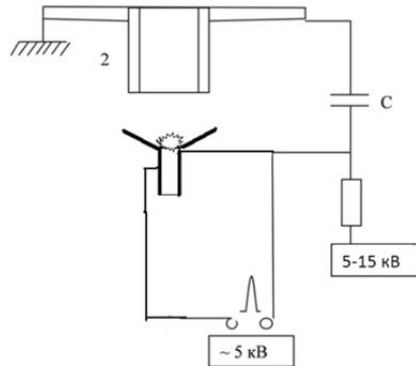


Figure S16. The design of the electron gun. 1 - cathode, 2 - anode.

A capacitor C was placed between the anode and cathode, charged from a high voltage source up to 5–15 kV. At the moment of breakdown, the energy of the capacitor C was expended on accelerating electrons from the breakdown plasma. Between pulses, capacitance C was recharged from a high-voltage source with a the time constant $RC \sim 1$ ms. Note that the total duration of the current depended on the time of development and existence of the discharge plasma over the ferroelectric surface and the time of the discharge of the capacitor C through the plasma bunch formed as a result of breakdown over the surface. This time, in particular, depends on both the plasma parameters and the capacitance C and parasitic parameters determined by the design of the discharge gap.

C. Control of parameters of e-beam

The pulsed e-beam was not strictly monochromatic, although most of the electrons had a maximum energy determined by the 12.5 kV voltage on the charged capacitor C . As this capacitor was discharged during the pulse time, the voltage across it and, accordingly, the intensity of the accelerating field decreased. In our experiments, a diaphragm with a typical diameter of 4 mm was installed in front of the sample, which limited the size of the irradiated region of the sample. To measure the current of the electron beam incident on the sample, we used a custom design developed for this purpose (see Figure S17). The e-beam was formed in the plane of the sample using magnetic lenses and a deflecting system. It is known that the focal length of magnetic lenses depends on the energy of electrons. If the beam is not strictly monoenergetic, then electrons with different energies are focused on different distances. In this case, since the emissivity of the cathode increases with increasing accelerating voltage, most of the electrons have a maximum energy. When adjusting magnetic lenses by adjusting the current through them to obtain the maximum e-current, the latter is focused on the plane of the diaphragm in front of the sample. Electrons with lower energy are focused on other planes, and only a part of them flies through the diaphragm. Thus, the diaphragm in front of

the sample is an energy selector of electrons: the smaller its size, the more monoenergetic the electron beam will be. Accordingly, the total duration of the e-beam current pulse in the case of a non-monoenergetic beam, will depend on the diameter of the diaphragm.

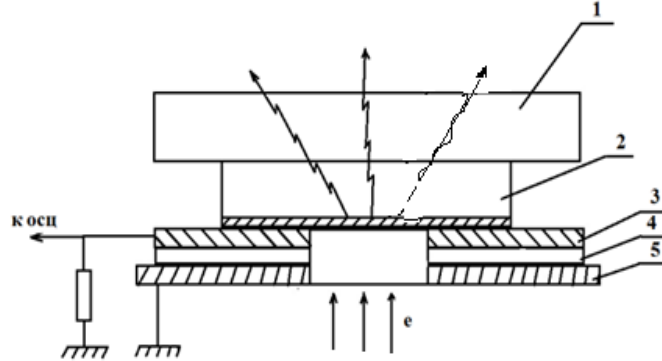


Figure S17. Scheme for measuring the electron beam current (pump current). 1 – sapphire window of the vacuum chamber, 2 – sample with a deposited Al-layer, 3 – diaphragm made of soft metal (indium), 4 – insulator (mica), 5 – copper diaphragm. Figure S18 shows three typical pulses of the e-beam current with a total pulse duration of 0.4-0.5 μ s each, which consisted of an irregular sequence of series of short pulses with a duration from \sim 1 ns to tens of nanoseconds with a different shape.

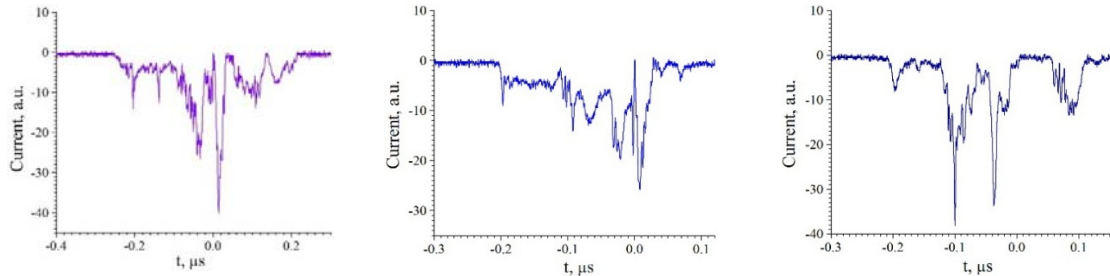


Figure S18. Typical e-beam current pulses measured for several discharges with a 4 mm diaphragm.

Apparently, the shape and magnitude of the current pulses depended both on the specific state of the discharge gap near the ferroelectric surface and on the magnitude of the magnetic field in the focusing and deflecting coils. Since the samples of GaN/AlN MQW structures were grown on *c*-sapphire dielectric substrates, this led to significant electric charging excited by an *e*-beam exacerbated by the high pulsed beam currents used (up to several amperes). To eliminate charging-induced measurement artifacts and prevent a potential dielectric breakdown of the samples, a thin conductive aluminum (Al) film was deposited on their surface. Due to the relatively high reflection coefficient of Al in the UVC range (>80%), this coating also reflected part of the UVC radiation from the structure towards the substrate.

The e-beam current passed through the diaphragm and absorbed by the sample passed through a $50\ \Omega$ resistor placed outside the vacuum chamber, the voltage pulse across which was measured by a high-frequency oscilloscope like to Tektronix TDS3000B or MSO 4104 with a bandwidth of 350 MHz or 1 GHz, respectively.

D. Measurements of power characteristics of output UVC radiation

The sample under study was fixed directly on the exit window of the vacuum chamber with dimensions that ensured the minimum distance between the sample and the photodetector (~20 mm), as shown in Figure S15. In the work, we used a standard industrial photocell for recording short light pulses - a coaxial photocell FEK-22SPU with large-diameter photocathode, 40 mm (active area 12.6 cm^2).^[87] This element measured the optical power of light pulses in a wide solid angle and in the wide spectral range 220 - 650 nm with a time resolution of 0.5 ns. This photocell provides a sensitivity of $30\ \mu\text{A/lm}$ in this spectral range with an upper limit of linearity of 18 A. For UVC-radiation with a wavelength of more than 270 nm, the sensitivity of the element is $17\ \text{mA/W}$, and in the range of 230-240 nm it slightly decreases to $15.5\text{--}16\ \text{mA/W}$ respectively. Figure S19 shows the schematic design of this photodetector and optical transmission spectrum of the output sapphire window of the camera, which shows that its transmittance in the range of 230–240 nm is 70–75%.

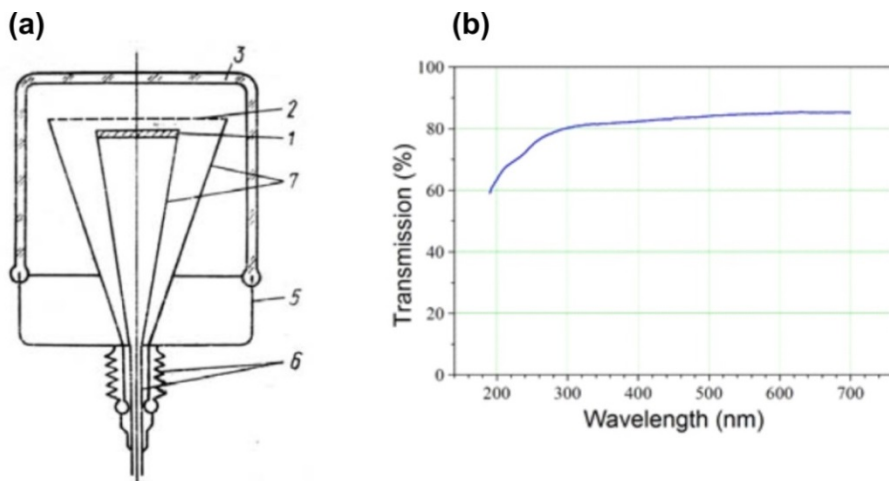


Figure S19. (a) Schematic design of photocell FEK-22SPU: 1 – photocathode, 2 - anode, 3 – input window, 5 – metallic body, 6- coaxial connector, 7- matching transition with equal impedance. (b) Optical transmission spectrum of the vacuum chamber window.

In addition, it should be taken into account that in the FEK-22SPU photocell, radiation enters the photocathode through the anode, made in the form of a "blind" - a set of thin metal plates, the plane of which is perpendicular to the flat surface of the photocathode. When measuring the spontaneous emission of structures, a significant fraction of the light passes at

large angles to the cathode surface and part of the radiation falls on the side surfaces of the anode plates, being partially absorbed by them, and the radiation loss depends on the angle of incidence of light on the photodetector. This issue was considered in detail in our first paper in 2015 on electron-pumped UVC emitters.^[S8]

Thus, the absolute values of the output optical power of GaN/AlN MQW structures were calibrated as mA/W taking into account all the above factors. In all our works since 2015 we use this type of photocell with a constant calibration.

E. Measurements of CL spectra excited by a high-current e-gun

Figure 5 show the CL spectra of the *F*-series structures measured. Due to the non-reproducible nature of each *e*-beam pumping pulse from *e*-gun with a plasma ferroelectric cathode, it was impossible to record emission spectra using standard spectrographs based on conventional photomultipliers and stepper motors, which were used for the measurements of all CL spectra excited by low-current *e*-beam. To measure the CL emission spectra excited by a high-current *e*-beam we used a miniature S100 spectrograph with a concave diffraction grating,[S9] and a CCD array for detection. The device provided measurements in the spectral range of 190 – 1100 nm with a resolution of 1 – 2 nm. The signal accumulation time was usually 10 – 20 seconds at a pulse repetition rate of 12 Hz. At a lower frequency (1.5 Hz), recording was possible only in the presence of intense luminescence, since noise increased correspondingly with an increase in the accumulation time.

References:

- S1. W. Sun, C.-K. Tan, N. Tansu, AlN/GaN Digital Alloy for Mid- and Deep-Ultraviolet Optoelectronics, *Sci. Rep.* 7, 11826. <https://doi.org/10.1038/s41598-017-12125-9>
- S2. G.I. Rosenman, V.A. Okh apkin, Yu.L. Chepelev, V.Ya. Shur, Electron emission at the switching of ferroelectric lead hermanate, *JETP Letters*, 39(9), (1984) 397. (in Russian)
- S3. B. Jiang, G. Kirkman, N. Reinhardt, High brightness electron beam produced by a ferroelectric cathode, *Appl. Phys. Lett.* 1995, 66, 1196-1198.
- S4. G. Rosenman D. Shur, Ya. E. Krasik and A. Dunaevsky, Electron emission from ferroelectrics, *J. Appl. Phys.* 88(11) (2000) 6109 – 6161.
- S5. M. Einat, E. Jerby, G. Rosenman, A ferroelectric electron gun in a free-electron maser experiment, *Nuclear Instruments and Methods in Physics Research A* 483 (2002) 326.
- S6. Mesyats, G.A. Electron emission from ferroelectric plasma cathodes, *Physics Uspekhi* 2008, 51(1), 79-100.
- S7. Baranochnikov M.L. Detectors of radiations. Handbook. Part 3. M.:DMK Press, 2012. - 640p., tab.415, ill.1326. ISBN 978-5-94074-564-8
- S8. S. V. Ivanov, V. N. Jmerik, D. V. Nechaev, V. I. Kozlovsky, M. D. Tiberi, E-beam pumped mid-UV sources based on MBE-grown AlGaN MQW, *Phys. Status Solidi A* 212(5) (2015) 1011–1016.
- S9. <https://solarlaser.com/en/>

Table content

The formation mechanisms of 2D-GaN quantum-dimensional ribbons and disks of subcritical thickness (<2 ML) in 250×GaN/AlN MQW structures grown by plasma-activated molecular beam epitaxy are investigated. Precise control of the nominal GaN thickness (± 0.25 ML) and growth conditions allowed us to demonstrate electron-beam-pumped UVC emitters operating in the 228–256 nm wavelength range with a peak optical power of 1 – 37 W, respectively.